Two Applications of Plasma Physics Modeling for Controlled Fusion Research

A thesis by Grant Rutherford presented for the degree of Bachelor of Science in Physics

Supervised by Professor Jonathan Pober

Department of Physics
Brown University
April 27, 2021

TABLE OF CONTENTS

Abstract

Presented in this thesis are two independent projects related to magnetically confined plasmas and controlled fusion. In the first project (Chapter 2), I constructed and solved a 0D model as an initial value problem to study startup of the Princeton Field Reversed Configuration-2 (PFRC-2), the second in a series of four experiments determining the viability of a compact aneutronic field-reversed configuration (FRC) reactor for use as a rocket engine or for electricity generation. The purpose of the model was to better understand the relative importance of different processes during startup and how initial conditions affect startup.

Incorporated into the model are hydrogen processes using collisional radiative rate coefficients taken from the EIRENE database, charged particle loss due to plasma flow parallel tothe magnetic field, enhanced confinement from the mirror field and the FRC, electron interactions with the ends of the machine and subsequent generation of nonthermal, high energy electrons. By solving the model I obtain the density and energy of the plasma species as a function of time. I then present trends of the electron density and energy in several parameters, including P_{in}, n_{H_2}, B. Additionally, I explore the effect of the high energy electrons on startup.

In the second project (Chapter 3), I simulated radio frequency (RF) electromagnetic waves to explore the feasibility of generating a density beat oscillation with high harmonic fast waves (HHFWs) and of measuring it numerically with 2D beam emission spectroscopy (BES) in the National Spherical Tokamak Experiment-Upgrade (NSTX-U), a spherical tokamak at the Princeton Plasma Physics Laboratory. The beat oscillation is of interest as it can be used to determine the RF fields of the device, an ability NSTX-U currently lacks, by comparing it against 3D RF calculations.

I began by computing HHFW fields in NSTX-U under a variety of experimental conditions and antenna configurations with Petra-M, a 3D RF wavefield solver. These fields were then used to evaluate the amplitude of $\delta n_{e,beat}/n_{e0}$ in the volume of measurement, the value of which is predicted to be between $5 \cdot 10^{-10}$ and 10^{-9}, though it is highly dependent on plasma parameters. Trends in magnetic field, core temperature, core density, and antenna phasing are presented, and the parameters most suitable to this measurement are identified. Finally, I developed a synthetic BES diagnostic to compare the experimental BES signal against.

In addition to the introductory section of each project provided in their respective chapter, additional relevant background is given in Chapter 1. If the reader is not familiar with plasma or controlled fusion, Sections 1.1-1.3 will be useful. Relevant to Chapter 2 are Section 1.3.2 for a discussion on aneutronic fuel and Section 1.4.1 for an explanation of FRCs and magnetic mirrors. Relevant to Chapter 3 are Section 1.4.1 for a primer on tokamaks, Section 1.5.2 for a discussion on neutral beams, and Section 1.5.3 for an introduction to how electromagnetic waves can interact with a plasma.

Chapter 1

Introduction[1]

1.1 Plasma

Plasma, also known as the fourth state of matter, is a gas whose particles have become ionized. Typically, ionization is a result of either heating a gas to high temperatures where inter-particle collisions are energetic enough to eject electrons or due to the presence of a strong electric field that accelerates free electrons into neutral particles at high enough speeds to ionize them. In either case, the resulting state of matter is a soup of electrons, positive ions (which are referred to simply as ions), and neutral particles. Each class of plasma particle is called a species (i.e. the electrons are a species, the ions are a species, etc.). It is worth noting that there may be multiple neutral or ion species depending on the starting gas.

Plasmas are similar to gases in many ways, but the presence of charged particles causes plasma to be sensitive to electric and magnetic fields and gives rise to many new phenomena. One such phenomenon is an important property of plasmas: quasi-neutrality. Because plasmas contain mobile charge carriers, regions may arise where the net charge is nonzero, leading to electric potentials that act upon the electrons and ions and seek to neutralize areas of net charge. Therefore, in many circumstances, it can be assumed that within a given plasma volume, $q_e n_e = -q_i n_i$, where q_e is the charge of an electron, n_e is the electron number density, q_i is the charge of an ion, and n_i is the ion number density. Many more phenomena will be discussed throughout the remainder of this thesis, but I hope that knowing of quasi-neutrality can begin to elucidate how complex plasma dynamics can be.

Beyond the intellectual interest in complex problems, studying plasmas has a tremendous number of wide-ranging applications, including astrophysics (stars, interstellar media, accretion disks, etc.), accelerator physics (wakefield acceleration), agriculture (anti-microbial agent, improving growth), and industry (neon signs, plasma torches, surface treatment, ion engines, etc.). All of these areas are important in their own right, but I believe the most important application of plasma is clean energy generation via controlled fusion.

1.2 Nuclear Fusion

Before discussing controlled fusion, let me introduce nuclear fusion. Nuclear fusion is a nuclear reaction between two nuclei that occurs when the distance between them is small enough

[1]The introduction to plasma physics presented in this chapter is largely an adapted version of Francis Chen's Introduction to Plasma Physics and Controlled Fusion [1] and Umran Inan and Marek Gołkowski's Principles of Plasma Physics for Engineers and Scientists [2]. Please see either text for more details.

(on the order of 10^{-15} m) that the strong force fuses them together into a single, new nucleus (which may or may not rapidly decay into several products). It is worth nothing that without nuclear fusion, we would not be here today. After Big Bang nucleosynthesis, no elements heavier than lithium existed in the universe. Such heavier elements were instead formed later via nuclear fusion in stars and stellar processes. Given that our bodies contain many elements heavier than lithium, humans would not exist without nuclear fusion.

Looking at one's surroundings, there is a plethora of elements heavier than lithium, so one may suspect that fusion occurs somewhat readily. However, this is not the case, and it is quite unlikely for nuclei to grow close enough to fuse, often requiring extreme conditions, like those at the center of a star. The difficulty of fusion arises as a result of the Coulomb force, specifically that it repels like-charges. Nuclei are often surrounded by a cloud of negatively charged electrons. This cloud is an order of magnitude wider in diameter than the nucleus, so the clouds of two approaching atoms will repel one another far before the nuclei are close enough to fuse. The most common solution to this problem is to first ionize all of the fusion reactants. However, nuclei are positively charged, so they too repel one another. But if the nuclei have high enough velocities, there is not enough time for the Coulomb force to repel the nuclei before they grow close enough to fuse. These high velocities are typically achieved by heating the fusion fuel to millions of degrees Celsius. The result of these two problems is that the fusion fuel is a high temperature ionized substance, i.e., a plasma.

Though not within the scope of this thesis, I should mention that there are several ways in which nuclear fusion may occur without using plasmas. One such example is muon catalyzed fusion, where the electrons of an atom are somehow replaced by muons. Muons are significantly heavier than electrons, so the muon cloud is much smaller than the electron cloud, allowing nuclei to fuse without needing to ionize them.[3] This has the advantage of not requiring the high temperatures of plasma-based approaches or the need to deal with the complexities associated with plasmas. Unfortunately, creating muons and replacing electrons with them is currently predicted to take more energy than the fusion reactions would produce. For the rest of this thesis, we will consider only plasma-based nuclear fusion.

1.3 Controlled Fusion

Controlled fusion is the process of using nuclear fusion to generate electricity. This is possible because when elements lighter than iron are fused, the product nuclei weigh less than the reactant nuclei, thereby releasing energy according to $E = \Delta mc^2$. Controlled fusion is a desirable power source for several reasons. First and foremost, none of the viable reactions for controlled fusion (see Sections 1.3.1 and 1.3.2) include carbon in any way, making controlled fusion carbon-free. Controlled fusion is also not intermittent, allowing it to provide baseload power, which will be highly useful for increasing grid stability as more and more electricity is generated via renewables. Additionally, fusion fuel has an incredibly high power density due to $E \propto c^2$. In fact, one gram of fusion fuel is equivalent to 56 barrels of crude oil. Some might question the need for controlled fusion since fission power is also a source of carbon-free, high power density baseload electricity. However, fission brings with it worries about runaway chain reactions, meltdowns, nuclear proliferation, and more. Controlled fusion, on the other hand, cannot suffer a runaway chain reaction nor a meltdown. And the risk of nuclear proliferation is substantially smaller.

There are of course disadvantages of controlled fusion or it would already be widespread. Easily the biggest disadvantage is that no reactor has been able to produce more electricity than

it takes to sustain the fusion reaction. There is a great deal of work being done to solve this issue, and the recent maturation of high-temperature superconductors has opened new pathways to better reactor performance by making higher magnetic fields accessible.[4] Another disadvantage is the cost. A large portion of this comes from previously needing to the build the reactors quite large, but with the higher magnetic fields, reactor designs are now trending towards smaller devices. However, they will still be somewhat expensive to construct, and the maintenance costs may be substantial. Additional advantages and disadvantages of controlled fusion come from the choice of reaction. There are only a handful of reactions that are viable for energy production, and they can be grouped into two categories: neutronic and aneutronic.

1.3.1 Neutronic Reactions

Neutronic fusion reactions are those which produce a neutron, such as

$$\mathrm{D} + \mathrm{T} \rightarrow \mathrm{n}(14.1\ \mathrm{MeV}) + {}^{4}\mathrm{He}(3.1\ \mathrm{MeV}) \tag{1.1}$$

$$\mathrm{D} + \mathrm{D} \rightarrow \mathrm{T}(1.01\ \mathrm{MeV}) + \mathrm{p}^{+}(3.02\ \mathrm{MeV}) \qquad 50\%\ \text{chance} \tag{1.2}$$

$$\rightarrow {}^{3}\mathrm{He}(0.82\ \mathrm{MeV}) + \mathrm{n}(2.45\ \mathrm{MeV}) \qquad 50\%\ \text{chance}, \tag{1.3}$$

where D is deuterium (an isotope of hydrogen with one neutron) and T is tritium (an isotope of hydrogen with two neutrons). Neutrons produced by these reactions will irradiate portions of the fusion reactor over time, decreasing the lifetime of the reactor components and creating short-lived radioactive waste. It should be stressed, though, that the radioactive waste produced by neutronic fusion reactions is very different from that produced by fission reactors. Whereas portions of fission waste remain radioactive for several hundred thousand years, fusion waste is able to be recycled or reused within one hundred years.[5] Thus, the infrastructure for storing fusion waste would be far simpler than that of fission waste. But any requirement of storage will raise the cost of neutronic fusion. And this cost is further increased by the need to replace reactor components more rapidly and to likely have to do so with some form of automation due to the radioactivity. Those who tolerate the material degradation and radioactivity do so because the D-T reaction has the highest reactivity out of all fusion reactions. It is for this reason that the first generation of fusion reactors will likely use the D-T reaction.

The reactivity of a fusion reaction is a measure of how likely that fusion reaction is to occur. A high reactivity is desirable because the amount of energy produced by a fusion reactor is proportional to the number of fusion reactions per second. Thus, the higher the reactivity, the more energy is produced and the more economical the reactor becomes. Fig 1.1 compares the reactivity of several different fusion reactions. The D-^{3}He and p-^{11}B reactions are aneutronic reactions and will discussed in the next section. The y axis label of this plot - Rate Coefficient - is another name for reactivity, and the x axis can be multiplied by about 11 million Celsius or Kelvin to get the temperature in units one may be accustomed to. A modern fusion reactor operates with a core plasma temperature of somewhere between 10 and 30 keV (around 100 million to 300 million K). Within this range, the rate coefficient for D-T is far higher than that of any other reaction. D-^{3}He reactors would need temperatures above 50 keV and p-^{11}B reactors would need temperatures above 100 keV to obtain the same reactivity of D-T at 10 keV. These high temperatures are not impossible to reach, but they bring with them their own challenges.

Another advantage of the D-T reaction is the abundance of deuterium on Earth. Around 1/80,000 of sea water is deuterium, and due to Earth's wealth of sea water, there is enough deuterium in the ocean to fuel widespread usage of fusion for hundreds of thousands of years.

Tritium, on the other hand, is radioactive with a half life of 12.3 years and is much rarer on Earth. Current stores of tritium come from it being a byproduct of certain types of fission reactors as well as being purposefully bred in other fission reactors, but these stockpiles are nowhere near large enough to fuel a fusion power plant long-term. Thankfully, a fusion reactor can generate its own source of tritium and would only need an outside source to begin operation.

Beyond irradiating the reactor and, as I will discuss later, being a means to extract energy from the plasma, neutrons can also produce tritium via collisions with lithium atoms via:

$$^{6}\mathrm{Li} + \mathrm{n} \rightarrow ^{4}\mathrm{He} + \mathrm{T} + 4.78\ \mathrm{MeV} \tag{1.4}$$

$$^{7}\mathrm{Li} + \mathrm{n} \rightarrow ^{4}\mathrm{He} + \mathrm{n} - 2.47\ \mathrm{MeV} \tag{1.5}$$

$$^{7}\mathrm{Li} + \mathrm{n} \rightarrow 2\mathrm{T} + 2\mathrm{n} - 10.3\ \mathrm{MeV}. \tag{1.6}$$

Therefore, if we surround the plasma with a material containing lithium, tritium will be produced. This region of tritium production is known as the breeding blanket. Because the D-T reaction produces one neutron for each tritium atom and because neutrons have a finite chance to not complete one of the above reactions and therefore not generate a tritium atom, the amount of tritium will continually trend downwards. To combat this, neutron multipliers, such as beryllium, are added to the blanket. When a neutron multiplier is struck by a neutron, it emits more than one neutron. Therefore, each fusion neutron may lead to additional neutron generation in the blanket, thereby increasing tritium production. If this production is large enough, excess tritium can be created and stored for use in a new fusion reactor.[6,7]

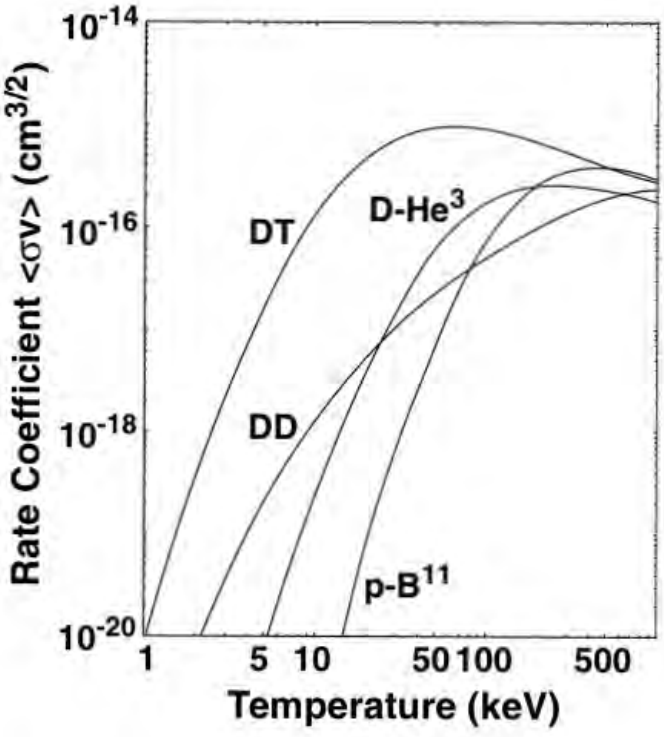

Figure 1.1: Rate coefficients (also known as reactivity) of important controlled fusion reactions as a function of keV. The x axis can be converted to Kelvin by multiplying the labels by about 11 million. [8]

1.3.2 Aneutronic Reactions

Some experts view the problems associated with radioactivity or tritium production as more trouble than the higher reactivity of the D-T reaction is worth and instead focus on aneutronic fusion reactions, those which do not produce neutrons. The two most popular aneutronic reactions are

$$\mathrm{D} + {}^3\mathrm{He} \rightarrow {}^4\mathrm{He}(3.6\ \mathrm{MeV}) + {}^1\mathrm{H}(14.7\ \mathrm{MeV}) \tag{1.7}$$

$$\mathrm{p}^+ + {}^{11}\mathrm{B} \rightarrow 3\,{}^4\mathrm{He}(2.9\ \mathrm{MeV\ each}). \tag{1.8}$$

As noted in the previous section, to obtain reactivities similar to that of D-T, much higher temperatures are needed, and even then, the peak D-T reactivity is significantly larger than the peak reactivity of D-^{3}He or p-^{11}B. The first generation of aneutronic reactors will likely use the D-^{3}He reaction due to its higher reactivity at lower temperatures relative to p-^{11}B. Unfortunately, due to the presence of deuterium, the D-D reactions (Eq 1.2 and Eq 1.3) will inevitably occur. These two D-D reactions have a equal chance of occurring, and both are detrimental to the effort of avoiding neutrons. The first reaction generates tritium, which can then react with deuterium to produce a neutron. And the second reaction forms a neutron right away. One can suppress this issue by not having equal parts D and ^{3}He and instead having a greater portion of ^{3}He (a ratio of 4 to 1, for example). This lowers the amount of D-D reactions that are possible but also limits the number of D-^{3}He reactions, further decreasing the reactivity relative to D-T. There is also the question of where to obtain this fuel. As stated in the previous section, deuterium can be extracted from sea water, but ^{3}He, like tritium, is not plentiful on Earth. Almost all of the world's ^{3}He reserves come from the radioactive decay of tritium. Thus, widespread use of the D-^{3}He reaction would necessitate a large-scale tritium breeding program. Interestingly, the moon happens to be plentiful in ^{3}He, and some experts suggest that due to the high energy density of fusion fuel (mentioned in Section 1.1), it may become economical to mine the moon and shuttle ^{3}He down to Earth once space travel has matured somewhat.

Alternatively, one could instead switch to the p-^{11}B reaction. Protons and ^{11}B are both plentiful on Earth, and there are no side reactions which could form neutrons. The catch is that substantially higher temperatures are required to obtain the same reactivity. Such temperatures are not currently obtainable in a fusion reactor if one wishes to continue confining the plasma, but that is not to say it will be impossible in the future. As fusion technology continues to progress, the p-^{11}B reaction will hopefully become more and more viable.

1.4 Confinement

Once the fusion reaction is chosen, there are three main steps to controlled fusion: confining the plasma, heating the plasma, and extracting energy from the plasma. Let me begin with confining the plasma. Terrestrial fusion requires heating the fuel to temperatures on the order of $100,000,000$ Kelvin. At these incredible temperatures, the plasma needs to be confined in such a way that it does not touch its container. Otherwise, the plasma would destroy the container and confinement would be lost. There are two main approaches to this problem: magnetic confinement fusion and inertial confinement fusion.

1.4.1 Magnetic Confinement Fusion

As mentioned in Section 1.1, plasmas are able to interact with magnetic fields, giving rise to many new phenomena that are not exhibited by gases. One such phenomenon is that plasma particles spiral around magnetic field lines, and it is this property that can be exploited to confine plasmas. According to the $q\vec{v} \times \vec{B}$ term in the equation of motion of charged particles, the velocity parallel to the magnetic field $v_\parallel$ is unaffected by the presence of a magnetic field, but the velocity perpendicular to the magnetic field $v_\perp$ is continually modified such that for a uniform field, the motion of the particle in the plane orthogonal to the field lines is a circle centered on a field line. To be slightly more mathematical, consider a particle with charge q, mass m, parallel velocity $v_\parallel = 0$, and perpendicular velocity $v_\perp$ in the presence of a uniform magnetic field $\vec{B} = B\hat{z}$. Such a particle will be confined to the x-y plane and will orbit in a circle of radius $r_c = mv_\perp/|q|B$ and angular frequency $\omega_c = qB/m$. Of note is that the direction of this orbit is dependent on the sign of the charge. For a magnetic field pointing out of the page, ions will rotate clockwise and electrons counter-clockwise. The radius r_c is known as the cyclotron radius, gyroradius, or Larmor radius, and the frequency ω_c is known as the cyclotron frequency or gyrofrequency. See Fig 1.2 for the motion of an electron with $v_\parallel \neq 0$ in a uniform field.

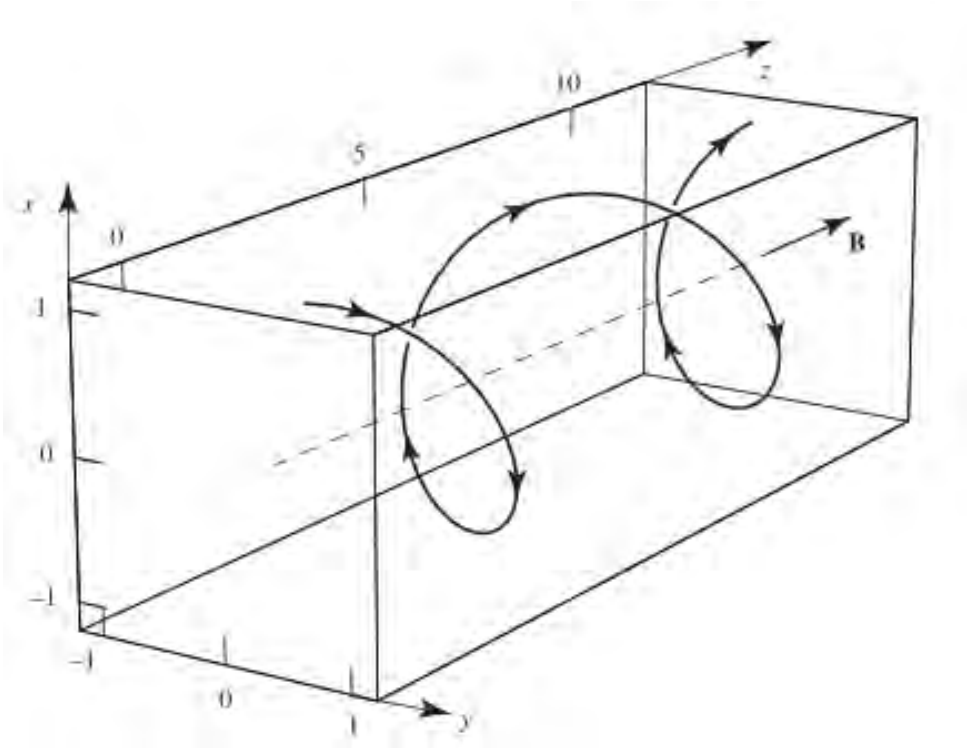

Figure 1.2: A negatively charged particle spiraling around a magnetic field line. [2]

From the previous paragraph, it would appear that a purely circular magnetic field would confine a plasma perfectly. Since the field lines loop back in on themselves and plasma follows field lines, the plasma should be confined in perpetuity by this method. However, the previous paragraph spoke only of a uniform magnetic field. In nonuniform magnetic fields, charged particles will experience drift motions as they spiral around the field lines. In the circular field lines example, the magnetic field in cylindrical coordinates is given by $\vec{B}(\vec{r}) = B(r)\hat{\theta}$, where $B(r)$ is a monotonically decreasing function due to engineering constraints. The relevant drifts are then the ∇B (Fig 1.3 a), finite-E (Fig 1.3 b), and curvature (Fig 1.3 c) drifts, which result

due to a non-zero gradient in the magnetic field, a finite electric field, and curvature of the magnetic field, respectively. The effects of these drifts are to modifying the motion of charged particles so that their motion perpendicular to the magnetic field is no longer a circle.

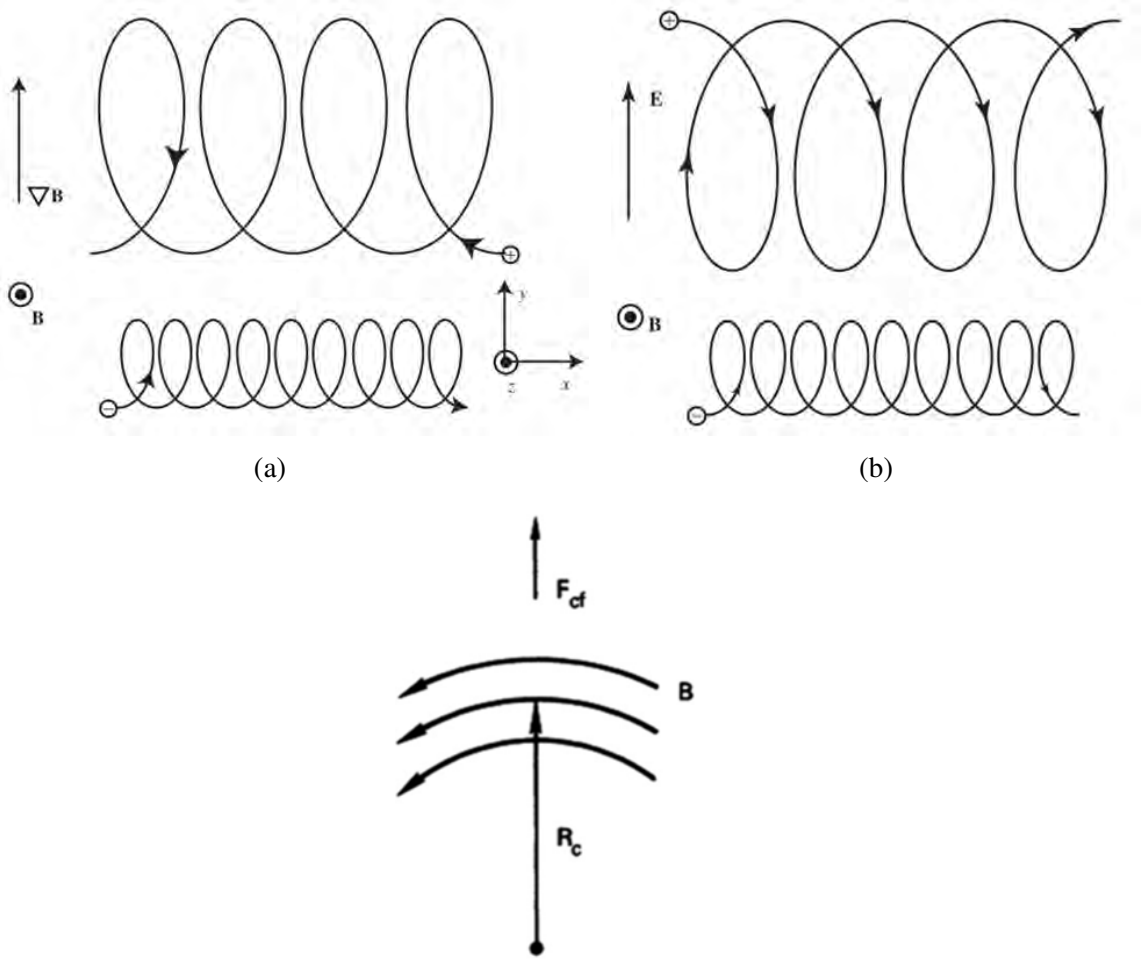

Figure 1.3: (a) Motions of an ion (top trajectory) and an electron (bottom trajectory) in the presence of a magnetic field with a constant, nonzero ∇B. (b) Motions of an ion (top trajectory) and an electron (bottom trajectory) in the presence of an electric field perpendicular to the magnetic field.[2] (c) As a charged particle spirals around a curving magnetic field line, it feels a centrifugal force $\mathbf{F_{cf}}$. Due to the cross product in their equations of motion, this force causes particles to drift either in or out of the page, depending on their charge.[1]

For circular field lines, the curvature and grad-B drifts combine to give a drift velocity of

$$\vec{v}_{\nabla B+\text{curve}} = \frac{m}{q}\frac{\vec{R}_c \times \vec{B}}{R_c^2 B^2}(v_\parallel^2 + \frac{1}{2}v_\perp^2), \tag{1.9}$$

where R_c is the radius of curvature. If the center of the circle is at the origin, the radius of curvature is simply the radial position vector. The important part of this drift velocity is its direction, specifically that it is dependent on the sign of the charge. Using the right hand rule and assuming a counter-clockwise magnetic field in the plane of the page, it is found that ions will rise out of the page and electrons will fall into the page. Thus, the charges separate and

form an electric field. The finite-E drift then becomes relevant and further modifies the particle orbits by

$$\vec{v}_E = \frac{\vec{E} \times \vec{B}}{B^2}. \tag{1.10}$$

Using the right hand rule once again with the electric field directed into the page, this new drift forces both ions and electrons towards the outer wall of the reactor. Thus, a purely circular field will always cause particles to drift outwards and therefore cannot be used to confine a plasma. Instead, more complicated magnetic field configurations are required that cancel out drift motions.[1,2]

Tokamaks

The Tokamak is one such configuration, and is current the most successful reactor design. Tokamaks were invented by the Soviet Union in 1958, with the name coming from a Russian acronym for "toroidal chamber with magnetic coils". They use helical field lines bent into a torus to confine the plasma, as shown in the schematic of Fig 1.4. Such an arrangement of magnetic fields is achieved through the combination of a toroidal (long way around the torus) magnetic field and a poloidal (short way around the torus) magnetic field. The toroidal field is generated by large superconducting magnets (blue in Fig 1.4). The poloidal field is generated by inducing a toroidal electrical current in the plasma. From Ampere's law, this in turn creates our desired poloidal field.[9,10] Most often, this plasma current is driven via induction. A solenoid placed at the center of the tokamak either monotonically increases or decreases its voltage, and the varying magnetic field creates a current in the plasma according to Faraday's law. The issue with this method is that the power supply for the solenoid can only ramp up the voltage so high (or low), thereby limiting the pulse length - the amount of time a reactor can continuously operate before resetting. The less time a tokamak is able to operate, fewer fusion reactions occur, making the device less economical.[10] It would be ideal if this quirk could be eliminated, so alternative ways to drive current, such as with electromagnetic waves or helicity injection, are under investigation. The mechanisms for both of these processes are outside the scope of the paper, but see these papers for wave current drive and helicity current drive: Fisch (1987) [11] and Bongard et al. (2019) [12]. Tokamaks do have a source of free current known as the bootstrap current, but an additional source of current is still required.[1]

Unfortunately, there are difficulties related to the plasma current regardless if it is driven inductively or non-inductively. Power plant-scale tokamaks require very large currents (around 8-15 MA), which in turn means a large amount of power is required to drive this current, leading to a high recirculating power. Recirculating power is the fraction of power generated by a fusion reactor that the machine uses to sustain itself. A smaller recirculating power allows for more power to enter the grid, making the reactor more economical. More worrisome than a high recirculating power are disruptions. Disruptions are events of complete loss of plasma confinement caused by instabilities in the plasma that arise due to the plasma current. All of the energy stored in the plasma and magnetic fields is suddenly deposited into the reactor, eroding the chamber walls and exerting tremendous stresses on the magnets.[10] Work is being done to tackle these issues, but some researchers feel as though tokamaks will never be viable power plants and instead look towards reactor designs that don't require a plasma current, such as the stellarator.

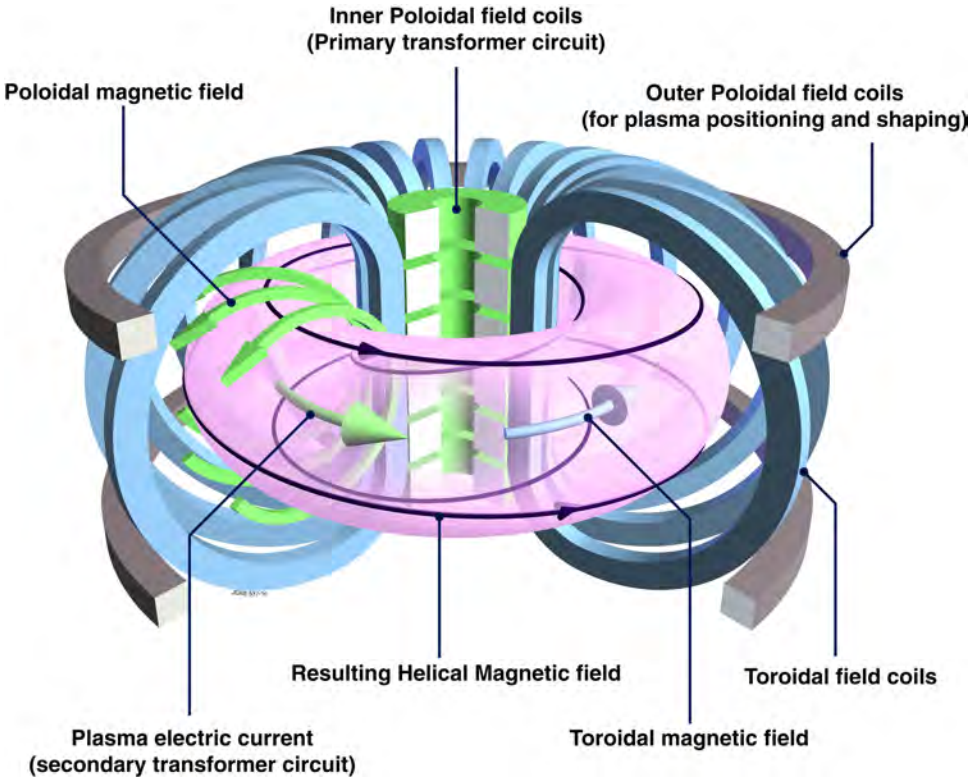

Figure 1.4: The tokamak magnetic confinement fusion reactor design.[13]

Stellarators

Invented at the Princeton Plasma Physics Laboratory in 1951, stellarators are another toroidal plasma configuration (see Fig 1.5).[14] Similar to tokamaks, stellarators also have twisting field lines, but instead of using a combination of superconducting electromagnets and a plasma current, their magnetic fields are formed entirely from electromagnets. To form such a field, elaborate, three dimensional magnets are used, which require state of the art software to design and high precision machining to build. It is for this reason that stellarators have historically had trouble performing at the same level as tokamaks. But recent advances in software and machining has lead to a resurgence of stellarators, and they may one day overtake tokamaks as the most successful reactor design.[15,16]

Magnetic mirrors

Though currently less favored than toroidal configurations, linear devices also exist. In fact, at the onset of fusion research in the 1940s, a linear configuration known as the magnetic mirror was one of the most popular reactor designs. Magnetic mirrors confine charged particles between regions of high magnetic field by exploiting the approximate conservation of magnetic moment (Fig 1.6) in a slowly varying magnetic field. The magnetic moment is given by $\mu = mv_\perp^2/2B$, where m is the particle mass, $v_\perp$ is the particle's velocity perpendicular to B, and B is the magnetic field. Conservation of this quantity dictates that as a particle moves into a higher-B region, $v_\perp$ must increase. Assuming a constant energy, as $v_\perp$ increases, the parallel velocity $v_\parallel$ must decrease. If the magnitude of the magnetic field at the ends of the mirror is large enough relative to the magnitude at the midplane, $v_\parallel$ will fall to 0 and then reverse directions, pushing the particle back into the low magnetic field region, where $v_\perp$ will decrease, allowing this process to repeat. The condition for confinement of a particle is given by $(M-1) > v_\parallel^2/v_\perp^2$,

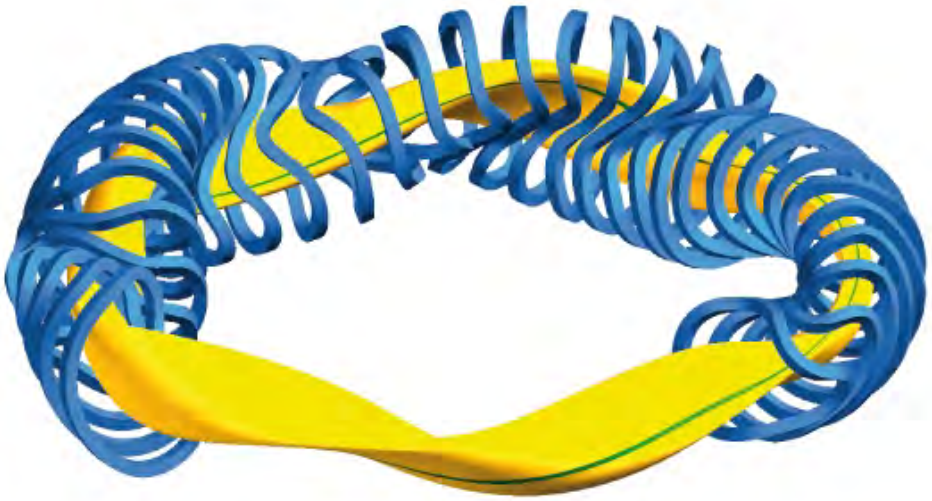

Figure 1.5: The stellarator magnetic confinement fusion reactor design. In blue are the electromagnets, in yellow is the plasma, and the green line is a single magnetic field line. [17]

where the velocities are taken to be at the midplane and the mirror ratio $M = B_{\text{end}}/B_{\text{mid}}$.[1,18] Though this configuration has largely fallen out of favor, continued work and technological advancements may bring magnetic mirrors back into vogue.[19]

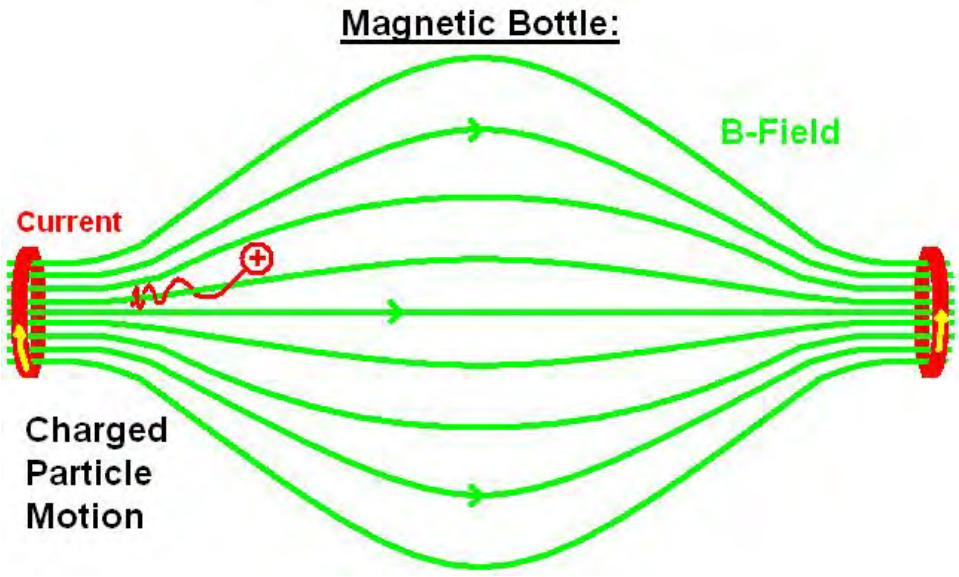

Figure 1.6: A simple magnetic mirror. In green are the magnetic field lines created by the electromagnets shown as red annuli. The partial trajectory of a positively charged particle is also illustrated. [20]

Field Reversed Configurations

Many more reactor designs exist, but it is unfortunately outside the scope of this thesis to discuss them all. Instead, I will focus on one last design that is somewhere between linear and toroidal: the field reversed configuration (FRC). FRCs are created by generating a circular

current in the presence of an axial magnetic field, where the current is directed such that the magnetic field created via Faraday's law opposes the direction of the original field on axis. Should this produced field have a large enough magnitude, there will be areas where the overall field reverses directions, forming an area of confinement in a shape similar to a tall donut.[1,21] See Fig 1.7 for a drawing of this configuration.

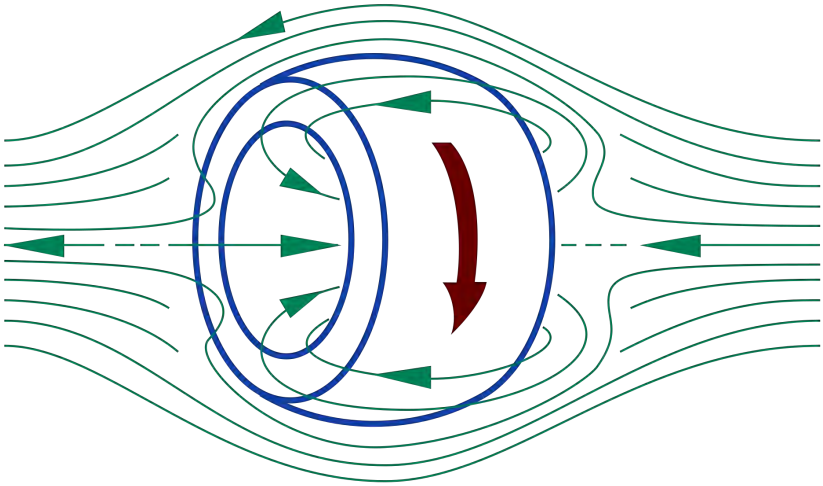

Figure 1.7: A field reversed configuration (FRC). In green are the magnetic field lines, in red is the plasma current, and the volume outlined in blue is the plasma. Notice that along the axis, the magnetic field reverses direction. [22]

1.4.2 Inertial Confinement Fusion

The other main approach to plasma confinement is inertial confinement fusion (ICF), which compresses a pellet of fusion fuel with such strength and speed than it fuses. Typically, the means of compression is an array of high powered lasers arranged symmetrically around the pellet. The stages of a ICF "shot" can be seen in Fig 1.8. First, photons hit the outermost layer of the pellet, heating it and turning it into plasma. Next, the newly formed hot plasma rapidly expands away from the pellet due to pressure gradients in the same way that a gas expands to fill a volume. From Newton's third law, this creates a large inward force on the pellet, compressing it to extreme pressures and heating it to hundreds of millions of degrees. Finally, the fusion reactions begin in the core and then spread throughout the pellet, thereby releasing energy.

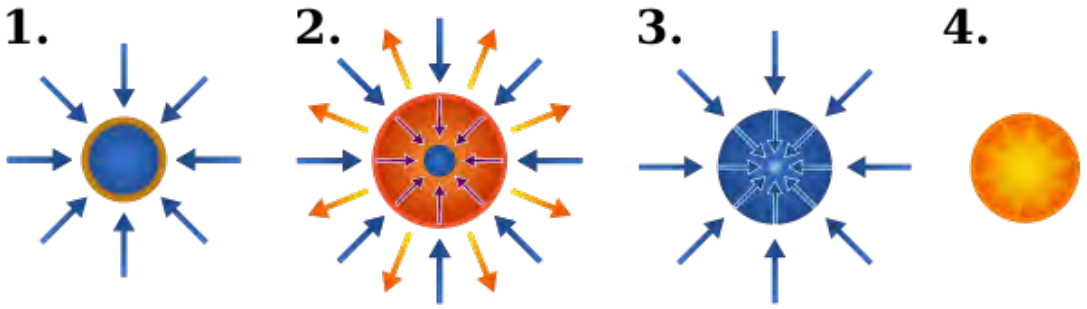

Figure 1.8: The four stages of an inertial confinement fusion shot. First, lasers heat the outermost layer of the pellet into a plasma. Second, the newly-formed plasma rapidly expands away from the pellet. Third, this expansion creates a reaction force that compresses and heats the pellet. Fourth and finally, the pellet reaches fusion conditions and energy is released. [23]

ICF can be divided into two main camps: direct drive and indirect drive. Direct drive ICF shines lasers directly onto the fuel pellet. This has the advantage of fewer sources of photon power loss, but the precision required for this method is far higher than indirect drive. Confining plasma has been likened to trying to hold Jell-O with rubber bands in that unless the plasma is symmetrically confined, it will escape through the areas of lesser confinement. Thus, for direct drive, great care is required to make as symmetrical a distribution of photon deposition as possible.[24]

Indirect drive instead shines the lasers on a holhraum with the pellet placed inside (see Fig 1.9). Hohlraums are hollowing cylinders that absorb photons before emitting that stored energy also in the form of photons (though at a different frequency). Hohlraums have the useful property that this new distribution of photons is smoother than the input distribution, thus partially correcting any asymmetries. But this benefit comes at a cost. Some of the energy of the original photon distribution is lost, thereby requiring more powerful (and therefore more expensive) lasers. Additionally, the hohlraum is not reusable, which makes each shot more expensive.[25]

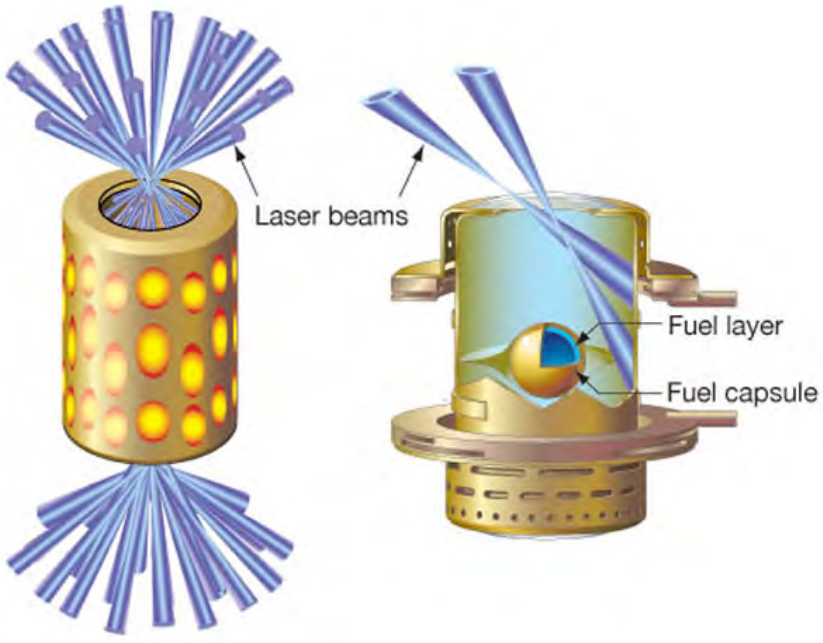

Figure 1.9: Hohlraum. [26]

Due to inefficiencies in laser amplification, low numbers of shots per second, and the necessity of extremely smooth fuel pellets for symmetrical compression, ICF is not widely considered a practical pathway to fusion energy. However, these issues are being address, and ICF may prove feasible in time. The remainder of this thesis will consider only magnetic confinement fusion.

1.5 Heating a Plasma

Once the confinement strategy is determined, the next step is to consider how to heat the plasma. Currently, the most common heating methods are ohmic heating, neutral beam injection, and wave-particle resonances. But as fusion reactors become more advanced and achieve a greater number of reactions per second, fusion product heating will play a larger and larger role. As will shortly be described, neutral beam injection and wave-particle resonances involve injecting either neutral particles or electromagnetic waves into the plasma, and for this reason they are referred to as external or auxiliary heating.

1.5.1 Ohmic Heating

Ohmic heating is the process of passing a current through the plasma to heat it. The mechanism behind this will be familiar to anyone who has taken an introductory E&M course. When a current travels through a resistive medium, some amount of that current is lost to the medium in the form of thermal energy according to $P = I^2R$. An interesting quirk of plasmas makes it so that ohmic heating cannot be the only source of heating. Unlike metals, which are more resistive at higher temperatures, the resistivity of a plasma $\propto T^{-3/2}$. Thus, as the temperature increases, a larger and larger current is required to provide the same amount of heating. At some point, that current is too large to be practical, and a new heating source becomes necessary. A more fundamental issues with ohmic heating is that it requires passing a current through the plasma. For certain confinement schemes, this is not an issue, but others are purposefully crafted to avoid the use of plasma currents, and thus ohmic heating is not available to those designs.

1.5.2 Neutral Beam Injection

Neutral beam injection (NBI) has historically been the most popular answer to the question of how to reach high temperatures. NBI launches a beam of highly energetic neutral particles into the plasma. These neutrals collide with plasma particles, and in each collision, some amount of their energy is shared with the plasma, thereby increasing its temperature. In order to not pollute the plasma with impurities, the injected neutrals are typically the same elements as the fuel particles. For example, in the case of the D-T reaction, a reactor with two neutral beams would likely use a deuterium neutral beam and a tritium neutral beam. The desired energy of these neutral beams depends on the reactor and its specific conditions, but it can range from 10 keV to 1 MeV

The process for creating a neutral beam can be seen in Fig 1.10. First, a gas is ionized to form a plasma. The ions of this plasma are then accelerated to high speeds via an electric field. As the ions stream towards the plasma, they encounter a neutral gas and via charge exchange, the ions obtain obtain electrons and form a neutral particle while still retaining their large kinetic energies. Any remaining ions are deflected away from the plasma using a magnetic

field, and any low energy neutrals are pumped out of the chamber. The result is a high energy beam of neutrals injected into the plasma.[27]

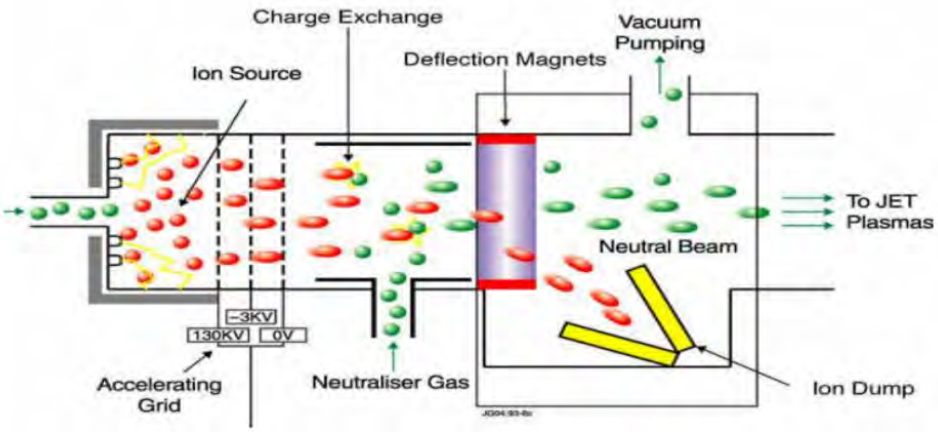

Figure 1.10: Diagram of the creation of a neutral beam for injection into a plasma. [27]

1.5.3 Wave-Particle Resonances

Another major external heating method is the use of wave-particle resonances. It might at first seem strange to heat something with waves, but this is actually a part of our daily lives. In a microwave oven, oscillating electromagnetic waves cause water molecules to rapidly rotate, thereby heating the food. One can consider wave-particle resonances to be a highly refined version of the same concept. A key difference is that whereas all microwave ovens operate basically identically, there are many different options for how we can heat a plasma with waves. For example, one could choose to heat the electrons, which will transfer that energy to the ions[2], or one could choose to heat the ions directly. Some resonances even heat both electrons and ions. Going through all of these resonances is outside the scope of this thesis, but I will describe the fundamental cyclotron resonance, which I find to be the most intuitive wave-particle interaction.

Consider a charged particle in a uniform magnetic field. As stated in Section 1.4.1, the motion of such a particle will trace a circle in the plane perpendicular to the field. Now suppose we introduce a circularly polarized electromagnetic wave (see Fig 1.11 for an example of such a wave) that propagates along the magnetic field. If the angular frequency of the electric field matches the cyclotron frequency $\omega_c = qB/m$ of the charged particle - the frequency at which the particle revolves around the magnetic field line - and the two are in phase, then the particle will feel a force that is constantly pulling it around the field line, thus increasing its perpendicular velocity. And because ω_c does not depend on $v_\perp$, the particle will remain phase matched to the wave, thereby continuously gaining kinetic energy, until some other plasma process affects the particle's gyrophase. In addition to heating plasmas, I should note that wave-particle resonances have other applications, such as driving current[11] or instability mitigation[28].

[2]At the end of the day, it is the ions we are interested in heating since they are the particles that need to reach extreme temperatures to fuse.

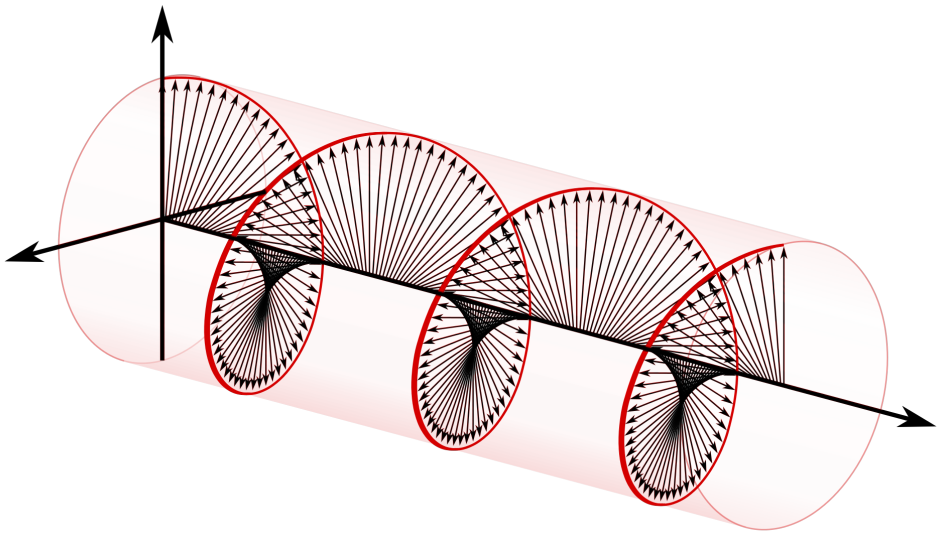

Figure 1.11: An example of a circularly polarized wave. [29]

1.5.4 Fusion Product Heating

The energy of fusion reactions is produced in the form of kinetic energy given to the product particles. Looking to the reactions listed in Sections 1.3.1 and 1.3.2, the energy of these particles are measured in MeV. Comparing this to the rest of the plasma, which has its energy measured in units keV (see Fig 1.1), it becomes clear that fusion products are highly energetic particles. If these particles are charged, they will be confined by the magnetic fields and remain in the plasma. Then, similar to the high energy neutrals particles of NBI, the fusion products will share their energy with the rest of the plasma via collisions. This process is typically considered for alpha particles as they are the only charged product created by the popular D-T reaction (see Section 1.3.1). In this case, the heating is referred to as alpha heating. Should enough fusion reactions occur per second, fusion products will deposit enough energy in the plasma that all external heating can be shut off. At this point, the fusion reaction is self-sustaining, much like a fire, and the plasma is said to have reached ignition.

1.6 Extracting Energy

Now that the plasma is confined and heated to fusion conditions, the energy from the fusion reactions needs to be extracted. The method of doing so depends on whether or not the fuel is neutronic. Being the more popular, I will begin with how to extract energy from a neutronic fusion reactor.

1.6.1 Neutronic Energy

The products of neutronic reactions are neutrons and charged particles. The charged products, due to having a non-zero charge, will be confined by the magnetic field (see Section 1.5.4) and remain in the plasma. The neutron, however, will fly off in some direction before eventually encountering the wall. The wall of a typical fusion reactor is made up of several layers, as shown in Fig 1.12. The layer closest to the plasma is designed to survive the high heat fluxes, is known as the first wall, and is thin enough that most neutrons will pass through it. The next

layer is the breeding blanket (see Section 1.3.1), and it is here that the energy extraction takes place. The blanket is thick enough that a large portion of neutrons will collide with the blanket material. As the neutrons collide, their high kinetic energies are converted into thermal energy of the surrounding material. A coolant is then pumped through the blanket to absorb this heat. The now-hot coolant is then used to spin a steam turbine and thus generate electricity. Beyond the breeding blanket is a radiation shield that protects both operators and the superconducting magnets from any neutrons that did not collide in the blanket.

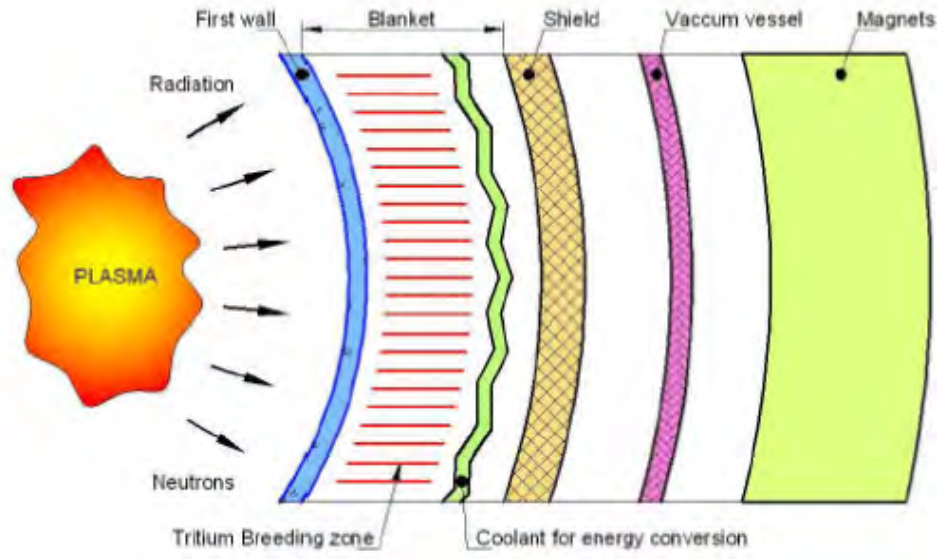

Figure 1.12: Schematic of a fusion reactor's wall. [30]

1.6.2 Aneutronic Energy

In an aneutronic fusion reactor, all fusion products are charged and are therefore confined by the magnetic field. Thus, the method of extracting energy from a neutronic reactor cannot be applied here. Instead, a process known as direct conversion is used. In direct conversion, the motion of charged particles creates a voltage in a wire, thereby generating electricity. This process is commonly seen in reverse (such as in the production of high energy neutral beams (Section 1.5.2)), where a voltage is used to accelerate a charged particle. The most effective way to generate the voltage from plasma particles varies between reactor designs and in general remains an open problem in the field. See Johansson (2003) [31] and Rosenbluth et al. (1994) [32] for more information.

Bibliography

[1] Francis Chen. *Introduction to Plasma Physics and Controlled Fusion*. Springer, (2016).

[2] Umran Inan and Marek Gołkowski. *Principles of Plasma Physics for Engineers and Scientists*. Cambridge University Press, (2010).

[3] F. C. FRANK. Nature, **160**,525–527, (1947).

[4] M Greenwald *et al.* *https://library.psfc*

.mit.edu/catalog/reports/2010/18rr/18rr002/18rr002_full.pdf.

[5] https://www.iter.org/sci/Fusion. Accessed: 2020-03-4.

[6] A.R Raffray *et al.* Journal of Nuclear Materials, **307-311**,21–30, (2002). ISSN 0022-3115.

[7] M. A. ABDOU others. NUCLEAR ENGINEERING AND TECHNOLOGY, **37**,401–422, (2005).

[8] R Paul Drake. *High-Energy-Density Physics*. Springer, (2006).

[9] L.A. Artsimovich. Nuclear Fusion, **12**, 215–252, (1972).

[10] https://mediacentral.princeton.edu/media/SULI_18Jun20_BBattaglia/1_r5hr9brn/13468191. Accessed: 2020-03-4.

[11] Nathaniel J. Fisch. Rev. Mod. Phys., **59**, 175–234, (1987).

[12] M.W. Bongard *et al.* Nuclear Fusion, **59**, 076003, (2019).

[13] EUROfusion. https://www.euro-fusion.org/news/detail/detail/News/tokamak-principle/.

[14] Lyman Spitzer. The Physics of Fluids, **1**, 253–264, (1958).

[15] https://mediacentral.princeton.edu/media/SULI_18Jun20_ABader/1_l15rbp3n/13468191. Accessed: 2020-03-4.

[16] https://www.pppl.gov/events/science-saturday-renaissance-stellarator-fusion-concept. Accessed: 2020-03-4.

[17] Kirsten Haupt. https://www.iter.org/newsline/-/3037.

[18] R.F. Post. Nuclear Fusion, **27**,1579–1739, (1987).

[19] Sarah Perdue. https://news.wisc.edu/physicists-to-improve-plasma-fusion-mirror-devices-with-5-million-grant/, (2020).

[20] WikiHelper2134. https://en.wikipedia.org/wiki/Magnetic_mirror.

[21] M. Tuszewsk. Nuclear Fusion, **28**,2033–2092, (1988).

[22] Tokamac. https://en.wikipedia.org/wiki/Field-reversed_configuration.

[23] Benjamin D. Esham. https://en.wikipedia.org/wiki/Inertial_confinement_fusion.

[24] R. S. Craxton *et al.* Physics of Plasmas, **22**,110501, (2015).

[25] John Lindl. Physics of Plasmas, **2**,3933–4024, (1995).

[26] Lawrence Livermore National Laboratory. https://lasers.llnl.gov/science/icf.

[27] Bob Pinsker. https://suli.pppl.gov/2020/course/Pinsker_Auxiliary%20heating%20talk%20for%20PPPL%20202006019.pdf, (2020).

[28] D. De Lazzari *et al.* Nuclear Fusion, **49**, 075002, (2009).

[29] Dave3457. https://en.wikipedia.org/wiki/Circular_polarization.

[30] A K Suri *et al.* Journal of Physics: Conference Series, **208**,012001, (2010).

[31] Markus Johansson. (2003).

[32] M N Rosenbluth and F L Hinton. Plasma Physics and Controlled Fusion, **36**,1255–1268, (1994).

Chapter 2

Modeling Atomic and Molecular Plasma Processes During Startup of PFRC-2[1]

2.1 Introduction

2.1.1 PFRC

The Princeton Field-Reversed Configuration (PFRC) is a novel magnetic confinement fusion reactor design under analysis at the Princeton Plasma Physics Laboratory. It is a linear device based on the field-reversed configuration scheme with additional confinement from a magnetic mirror (see Section 1.4.1). What makes the PFRC design unique is the presence of an odd-parity rotating magnetic field (RMF) that is used to heat the plasma and drive the current that generates the FRC. The RMF is a magnetic field rotating around the major axis of the device and pointing in the radial direction. The odd-parity portion of the name comes from the magnetic field experiencing a sign change at the midplane of the device. See Fig 2.1 for a drawing of an odd-parity RMF. Some previous devices have incorporated even-parity RMFs, which do not exhibit a sign change at the midplane, but in each case, the RMF lead to loss of confinement.[1]

PFRC plans to use the aneutronic D-^{3}He reaction (see Section 1.3.2). Thus, should PFRC prove to be a valid reactor design, the lack of neutron-related issues and the simple design will offer a cheaper and more engineeringly viable path to fusion energy than that predicted for tokamaks. In addition to energy generation, the PFRC design has applications as a rocket engine, where the energetic fusion products are ejected to provide thrust[2]. See Fig 2.2 for an example schematic of a PFRC-based rocket. In either application, the reactor will operate by passing a cool plasma over the hot, dense plasma contained by the FRC. The fusion products of the hot plasma will heat the cool plasma, which can then either be ejected at high speeds to produce thrust or the kinetic energy can be extracted (See Section 1.6.2) to produce electricity.

2.1.2 PFRC-2

A series of four devices is planned to determine the feasibility of PFRC. As of writing, the current device is PFRC-2, which is focused on investigating the heating of the ions.[3] For testing purposes, PFRC-2 uses a purely hydrogen plasma (instead of D-^{3}He plasma), so no

[1]This chapter is an adapted version of my summer 2020 DOE Science Undergraduate Laboratory Internship (SULI) report. This work was completed with the help of Eugene Evans and Prof. Sam Cohen.

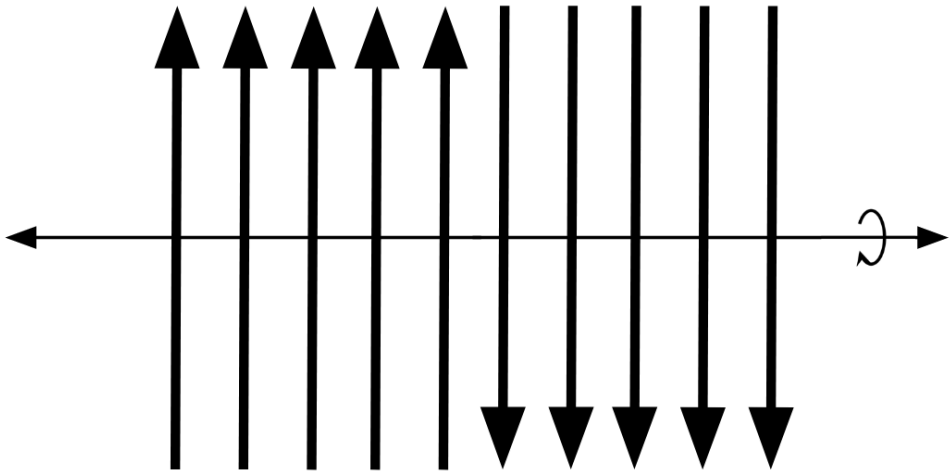

Figure 2.1: Example of an odd-parity rotating magnetic field (RMF)

fusion reactions will take place due to the low reactivity of protons. PFRC-2 is composed of three segments: the source end cell, the central cell, and the far end cell, as seen in Fig 2.3. Additionally in this figure are the mirror coils (in red) between segments that produce the magnetic mirror and the axial field coils (in green) that produce the axial field which will later be reversed in places to form the FRC.

A notable phenomenon discovered in PFRC-2 is a population of high energy electrons. These high energy electrons do not originate from the plasma but instead are generated via secondary electron emission when protons impact the end plates in the source end cell and far end cell. These plates have fluctuating electric potentials during operation and can become highly negative. If electrons are emitted when this is the case, those electrons will be accelerated to several keV, forming a population of electrons far more energetic than the bulk plasma electrons.[4] For the remainder of this chapter, I will refer to electrons originating in the plasma as low energy electrons.

2.1.3 Startup of PFRC-2

Startup of a fusion reactor is the process of going from no plasma being present in the machine to reaching steady state conditions. Depending on the reactor, this can take several different forms but invariably the fusion fuel begins in a gaseous state and must somehow be ionized. In the case of PFRC-2, the device is initially filled with H_2 gas and then a helicon antenna uses waves (Section 1.5.3) to ionize the gas in the source end cell to form a low density ($n_e \approx 10^9\,\mathrm{cm}^{-3}$) seed plasma. The seed plasma is then transported to the central cell for the purpose of giving the RMF something to couple to. This increases the consistency of startup and makes it proceed more rapidly.[5] The RMF then further heats the seed plasma, which ionizes gas in the central cell until the plasma reaches a density of $n_e \approx 10^{13}\,\mathrm{cm}^{-3}$. The process of going from the low density seed plasma to the higher density final plasma is known as densification and is what I sought to examine. Because I am only interested in the densification portion of startup, I focused on the central cell and began my simulations with the seed plasma already in place.

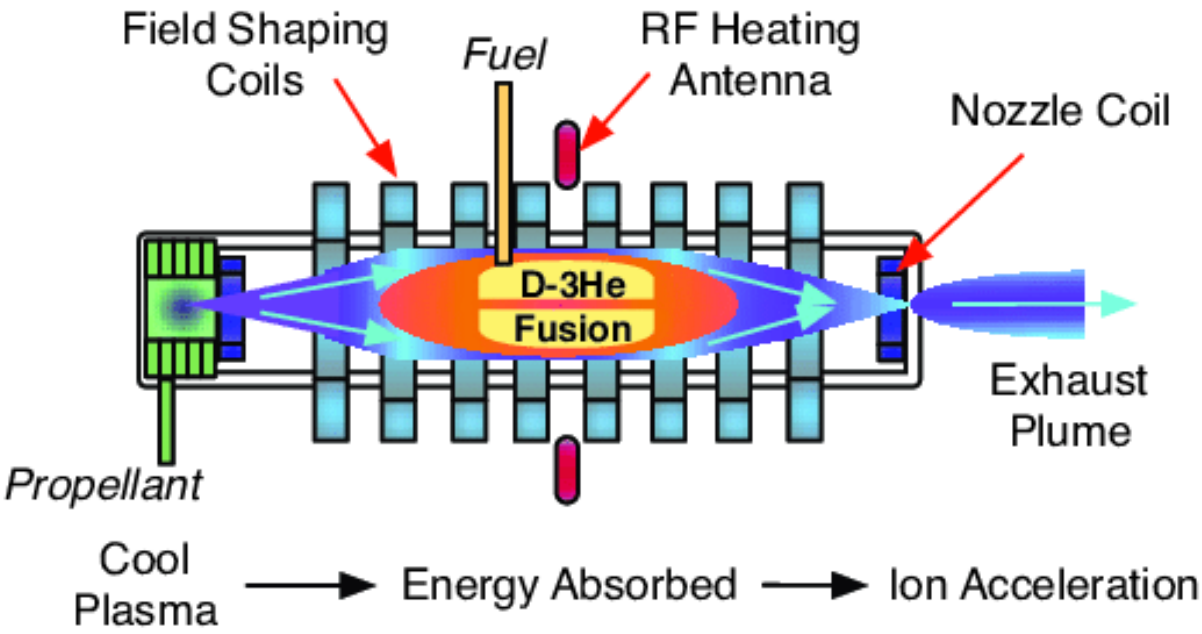

Figure 2.2: A schematic of what a PFRC-based rocket engine might look like

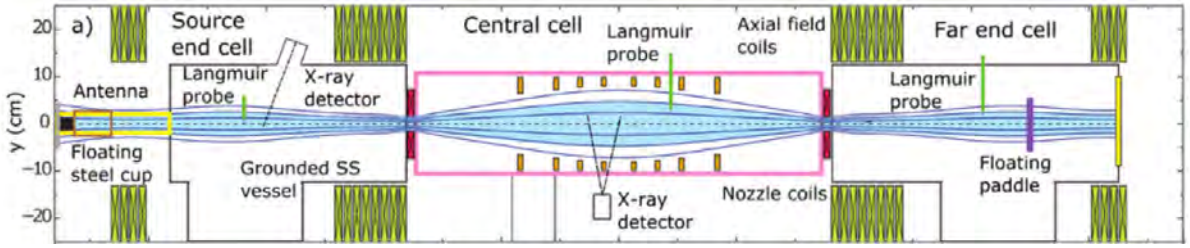

Figure 2.3: A schematic of PFRC-2 showing the three segments, the mirror coils (in red), and the axial field coils (in green).

2.2 Modeling Startup

The goals for this work were to better understand the general behavior of the plasma during densification, the relative importance of different processes, and the role that high energy electrons play in startup. To do so, I first constructed a model by evolving the number density n_s and total energy E_s of each species s (low energy electrons, high energy electrons, protons, atomic hydrogen, molecular hydrogen, and molecular ions) through time as according to ODEs for these quantities. These ODEs are functions of the various plasma processes incorporated into the model that will be discussed shortly. With the model in place I performed a series of parameter sweeps to identify how different processes affect densification. Sweeps over three of the most important parameters (which also happen to be controllable experimentally) - RMF power, initial fill density, and magnetic field strength - were performed both with and without high energy electrons to elucidate how the electrons interact with the bulk plasma. An additional goal of this work was to better understand the two timescales of densification. See Section 2.2.4 for an explanation of this phenomenon and how it was incorporated into the model.

Due to the complexity of startup and a limited time frame in which to complete the project, a number of simplifications are present in the model. The most important being that the model

is a 0D model. Thus, there is no spatial dimension, and instead the model can be thought to be predicting the dynamics of a 1 cm^3 portion of an infinite homogeneous plasma. Because of this, I cannot model spatial gradients, and processes that are a function of spatial effects use approximated parameters. I therefore was unable to model the FRC and instead estimated its effects on startup.

Other simplifications include excited states of neutral particles being wrapped into the rate coefficients of the various plasma processes; assuming the magnetic moment is adiabatic for mirror trapped (see Section 1.4.1) particles; assuming that all distributions are Maxwellian; assuming the plasma is cylindrical in shape; and having no delay between a particle leaving the plasma via Bohm diffusion (see Section 2.2.2) and either scattering back into the plasma or returning as a recycled neutral (see Section 2.2.3). Additionally, I do not allow the temperature of the high energy electron population to vary as a high energy electron does not remain in the plasma long enough for its energy to change appreciably.

Incorporated into the model are many plasma processes. Those that involve reactions are listed in Table 2.1. The rate coefficients for these processes were generated by a collisional radiative model obtained from the EIRENE code's atomic/molecular physics database (*http://www.eirene.de*). Additional processes are listed in Table 2.2. I will now discuss some of these additional processes in greater detail.

Process:	**Reaction:**
Ionization	$e + H \rightarrow 2e + p$ $H_2 + e \rightarrow H_2^+ + 2e$
Dissociative ionization	$H_2 + e \rightarrow H + p + 2e$ $H_2^+ + e \rightarrow 2p + 2e$
Recombination	$p + e \rightarrow H$
Dissociative recombination	$H_2^+ + e \rightarrow 2H$
Dissociation	$H_2 + e \rightarrow 2H + e$ $H_2^+ + e \rightarrow H + p + e$
Charge exchange	$H_2 + p \leftrightarrow H_2^+ + H$ $H + p \rightarrow p + H$

Table 2.1: Reaction-based processes in the model

Process:
Axial losses, reduced by mirror effects
Bohm losses
Bremsstrahlung losses
Changing radius
H_2 gas puffs
Helicon and RMF heating
Recycling and collisions with the chamber
Restorative influx of H_2 gas
Thermalization between particle species

Table 2.2: Additional processes included in the model

2.2.1 Axial Losses

Some portion of the charged particles in the central cell are continually lost as they flow along the magnetic field into other segments. Electrons are far less massive than ions and therefore have a much higher velocity. Electrons thus flow along field lines faster and are thereby lost more rapidly than the ions. This imbalance in loss rate produces charge imbalances in the plasma, leading to the development of electric potentials. These potentials increase the ion loss rate and decrease the electron loss rate until they are equal[2]. In the case of PFRC-2, it is assumed that both ions and electrons are traveling at the ion sound speed when this occurs. The ion sound speed is given by $c_s = (T_e \gamma Z k_b / m_i)^{1/2}$, where T_e is the electron temperature, γ is the adiabatic index, $Z = q_i/q_{\text{proton}}$, k_B is the Boltzmann constant, and m_i is the mass of the ion. Using that velocity together with a length scale ℓ_{plasma}, which I have chosen to be half the length of the plasma, an approximate flux of ions and electrons out of the central cell can be defined by

$$\Gamma_{\text{ax loss, i}} = \frac{c_{s,i} n_i}{\ell_{\text{plasma}}} \tag{2.1a}$$

$$\Gamma_{\text{ax loss, e}} = \sum_{i}^{\text{ions}} \Gamma_{\text{ax loss, i}}. \tag{2.1b}$$

However, there is also the effect of the mirror field leading to some portion of particles that would be lost instead bouncing back into the central cell. Assuming the magnetic moment of particles is adiabatic, a mirror ratio M = $B_{\text{end}}/B_{\text{midplane}}$ of 5, $v_\perp$ = $v_\parallel$ at the midplane, and a Maxwellian distribution of particle velocities, the magnetic mirror confinement condition $(M-1) > v_\parallel^2/v_\perp^2$ shows that 10.6% of particles are not reflected by the mirror and escape. The FRC also provides some additional confinement, which is incorporated via a reducing factor, r_{reducing}. Note that a smaller reducing factor provides greater confinement. r_{reducing} was set to 0.25 as it was found that some larger values did not provide enough confinement for maximum ionization to be reached. The final axial loss terms are then

$$\Gamma_{\text{ax loss, i}} = \frac{r_{\text{reducing}} \cdot m_{\text{escape}} \cdot c_{s,i} n_i}{\ell_{\text{plasma}}} \tag{2.2a}$$

$$\Gamma_{\text{ax loss, e}} = \sum_{i}^{\text{ions}} \Gamma_{\text{ax loss, i}}. \tag{2.2b}$$

2.2.2 Bohm Diffusion

Plasma particles, much like gas particles, seek to diffuse from regions of high number density to regions of low number density. Since the center of a plasma is the densest portion, particles will diffuse outwards towards the walls of the reactor. The magnetic fields confining a plasma greatly slow the rate of diffusion because it is difficult for charged particles to diffuse perpendicular to field lines, but diffusion cannot be completely halted.[6] The rate of diffusion is hard to predict and depends on the fusion reactor design in question. For PFRC-2, we assumed Bohm diffusion, which gives a diffusion coefficient of $D_{\text{Bohm}} = \frac{1}{16} k_B T/eB$. The flux of ions leaving the plasma is then

$$\Gamma_{\text{Bohm, i}} = r_{\text{recyc}} D_{\text{Bohm}} \mathrm{A}_{\text{plasma, nec}} \nabla n_e, \tag{2.3}$$

[2]This is one of the many outcomes of quasi-neutrality (see Section 1.1).

where r_{recyc} is the recycling coefficient, $A_{\text{plasma, nec}}$ is area of the plasma cylinder without end-caps, and ∇n_e is evaluated at the radius of the plasma. The recycling coefficient is the fraction of particles lost to the wall that recycle and will be discussed in the next section. To maintain quasi-neutrality (see Section1.1), electrons must also be lost according to

$$\Gamma_{\text{Bohm, e}} = \sum_{i}^{\text{ions}} \Gamma_{\text{Bohm, i}}. \tag{2.4}$$

2.2.3 Recycling and Collisions with the Chamber Wall

Recycling is the process where ions lost from the plasma will contact the wall, recombine, and then return to the plasma. These newly recombined neutrals will be reionized and lost to the wall again at some later point in time, hence the name recycling. A high level of recycling is detrimental to the operation of a fusion reactor because the newly recombined particles often do not penetrate far into the plasma when they return, instead being constrained to the edge of the plasma. The temperature of the plasma edge is too cold for fusion reactions to occur, and thus recycled particles cannot contribute to the energy generation. Furthermore, each ionization event saps a small amount of energy out of the plasma, cooling it. Repeated ionizations in the plasma edge can lead to a significant decrease in temperature, and while this at first does not seem problematic since the edge is already too cold for fusion, it has been found that the core and edge are coupled. By cooling the edge, the core (where fusion reactions do occur) is also cooled. An additional issue raised by recycling is that repeated bombardment of the reactor wall by highly energetic charged particles decreases the lifetime of the walls and can introduce impurities into the plasma. Therefore, recycling is aimed to be minimized.

The assumed source of recycled particles was Bohm diffusion. However, not all particles lost from the plasma will be recycled. Some will instead collide with the chamber and immediately bounce back into the plasma without recombining. I chose to arbitrarily set to fraction of particles lost that are recycled, r_{recyc}, to be 0.5. Because PFRC-2 is operating with a H_2 fill gas, the ions that can be recycled are protons and molecular ions, H_2^+. Protons are assumed to have equal probabilities of recombining into H or H_2 while molecular ions will only recombine into H_2. Newly-formed H particles are returned to the plasma with an energy of 0.5 eV whereas newly-formed H_2 particles are given an energy of 0.038 eV $= \frac{3}{2}T_{\text{room}}$. This lower energy is due to the lengthier process of forming an H_2 particle, giving them adequate time to thermalize with the room-temperature wall.

In addition to ions colliding with the wall and scattering back into the plasma, neutral particles may also do so. Molecular hydrogen will always scatter off the wall upon contact, but atomic hydrogen is assumed to be equally likely to immediately scatter as it is to form H_2 and then scatter. Whether an ion or a neutral, particles scattering off the wall will either gain energy or lose energy depending on their temperature relative to the wall. Specifically, the total energy of each scattered particle species is modified by $dE_{\text{s, total}}/dt = n_{\text{s,scatter}}(3/2)(T_{\text{room}} - T_s)\cdot\gamma$, where $n_{\text{s,scatter}}$ is the number of particles from species s scattering and γ is a free parameter currently set to 0.5.

2.2.4 Changing Radius

Experimentally, it is found that there are two timescales of densification. This phenomenon is illustrated in Fig 2.5, where the electron number density of three different PFRC-2 runs is plotted versus time (with $t = 0$ being the beginning of densification). It can been seen that

n_e increases proportionally to $e^{t/\tau}$, where τ takes on two distinct values τ_{slow} and τ_{fast}, before saturating and reaching steady state conditions. The naming of these time constants come from n_e increasing slower during the first portion of densification and increasing much more rapidly during the second. Though the exact cause of the two timescales of densification is unknown, one hypothesis is that the radius of the plasma shrinks due to increased confinement from the burgeoning FRC. The model investigates this hypothesis by initiating a radius change when the low energy electron density $n_{\text{e, low}} = 10^{11}$ cm^{-3}. At that point, the radius changes linearly from 6 cm to 3 cm over the course of 5 μs. Additionally, the plasma length decreases from 30 cm to 12 cm and the axial confinement increases by a factor of two over those 5 μs.

2.2.5 Helicon and RMF heating

The helicon antenna that produces the seed plasma (see Section 2.1.3) also deposits a constant amount of power into the simulated region given by

$$P_{\text{eff, helicon}} = V_{\text{sim}} \frac{1.6 \text{ W}}{V_{\text{helicon plasma}}}, \tag{2.5}$$

where V_{sim} is the volume of the simulated plasma (1 cm^3) and $V_{\text{helicon plasma}}$ is the volume of plasma stretching from the antenna in the source end cell through the central cell (2 meters long, $\sim$6 cm in radius). The helicon power is insignificant once RMF turns on, but prior to RMF, this term is responsible for maintaining steady state.

RMF heating is an integral part of PFRC-2's operation, so it is important to accurately model the RMF heating. That being said, I used a highly simplified model of the plasma-RMF coupling due to the exact dynamics not being fully understood. Using 20 kW as an approximate value for the maximum power the plasma can absorb and assuming that the absorbed power both scales with n_e and saturates close to $n_e = 5 \cdot 10^{12}$ cm^{-3}, the rate of energy transfer into the 1 cm cube (see Section 2.2) by the RMF is approximately

$$P_{\text{eff, RMF}} = V_{\text{sim}} \frac{20kW \cdot \min(\frac{n_e}{5 \cdot 10^{12}}, 1)}{V_{\text{plasma}}}, \tag{2.6}$$

where V_{plasma} is the volume of plasma just in the central cell.

2.2.6 Restorative Influx and Gas Puffs

There are two processes in PFRC-2 that provide additional H_2 to the plasma: a restorative influx and gas puffs. The restorative influx acts to restore n_{H_2} inside the plasma to its initial value pre-startup. This occurs because the plasma does not fill the full volume of the central cell (due to the confining magnetic field). The H_2 gas in the region outside of the plasma cylinder is therefore approximately non-ionized, leading to a greater concentration of H_2 outside the plasma than inside. Because the plasma is largely collisionless (due to its high temperature) the plasma does not significantly affect the equilibrium of the gas. Thus, the H_2 gas outside of the plasma diffuses into the plasma and seeks to return n_{H_2} to its initial value $n_{H_{2_0}}$. The flux of H_2 particles entering the plasma due to this effects is given by

$$\Gamma_{\text{restor}} = (n_{H_{2_0}} - n_{H_2}) v_{th} \frac{r_{\text{plasma}}}{\text{A}_{\text{plasma}}}, \tag{2.7}$$

where v_{th} is the thermal velocity of the gas, r_{plasma} is the radius of the plasma, and A_{plasma} is the area of the cylinder approximation that bounds the plasma

Gas puffs, on the other hand, are large, controlled influxes of H_2. Currently PFRC-2 does not operate with gas puffs during startup, but I was interested in seeing what effect they may have. In simulations where gas puffs are present, they are triggered when the combined total of the low and high energy electron number densities $n_e = n_{\text{e, low}} + n_{\text{e, high}} < 5 \cdot 10^{12}$ cm^{-3}. Gas puffs have a minimum length of 100 μs, a maximum length of 300 μs, and there is at least 150 μs between puffs. There is also a 50 μs delay between the trigger and gas reaching the plasma. Likewise, once a puff is stopped, it takes 50 μs for gas to stop entering the plasma. The puff influx was chosen semi-arbitrarily to be $5 \cdot 10^{16}$ cm$^{-3}s^{-1}$.

2.3 Results

Unless stated otherwise, all simulations were run with the parameters listed in Table 2.3. Additional free parameter values related to specific processes are described in the prior section.

Parameter:	**Value:**
Magnetic field strength	$B = 200$ G
Gas Puffs	Turned off
RMF turn on time	$t = 25$ μs
Initial fill pressure	0.5 mTorr
Initial low energy electron density	$n_{e_0,\text{ low}} = 6.98 \cdot 10^8$ cm^{-3}
Initial high energy electron density	$n_{e_0,\text{ high}} = 2.26 \cdot 10^6$ cm^{-3}
Kinetic energy of high energy electrons	750 eV
Initial proton density	$n_{p_0} = 6.3 \cdot 10^8$ cm^{-3}
Initial molecular ion density	$n_{H_{2\ 0}^+} = 7 \cdot 10^7$ cm^{-3}
Initial atomic hydrogen density	$n_{H_0} = 4.4 \cdot 10^8$ cm^{-3}
Initial molecular hydrogen density	$n_{H_{2_0}} = 1.65 \cdot 10^{13}$ cm^{-3}

Table 2.3: Some of the default simulation parameters. Additional free parameter values are given in Section 2.2.

2.3.1 General Behavior of the Model

Shown in Fig 2.4 is the result of a simulation run with the parameters described above. From $t = 0$ to $t = 25$ μs, no RMF is present and the plasma is maintained close to steady state by the helicon antenna. Once the RMF is turned on, there is a sharp rise in $T_{\text{e, low}}$ (dashed blue line) before it plateaus as the absorbed RMF power is balanced by ionization losses[7] and the addition of newly freed, colder electrons. When $n_{\text{e, low}}$ (solid blue line) hits 10^{11} cm^{-3} the radius change is triggered, and a second, faster timescale of densification is indeed produced. Interestingly, during the slow densification region, the molecular ions (solid gray line) are substantially more numerous than the protons (solid red line). However, in the fast densification region, the opposite is true. As of writing, it is unknown whether this phenomenon is physical or a quirk of the model.

While $n_{\text{e, low}}$ steadily increases throughout the slow densification region, $n_{\text{e, high}}$ (solid purple line) remains largely constant. It is not until the proton number density increases by several orders of magnitude that $n_{\text{e, high}}$ begins to significantly increase. This is because the creation of high energy electrons relies on protons flowing out of the central cell and contacting the end plates in the source end cell and far end cell. Furthermore, the secondary electron emission

produces a high energy electron only about 1 time in 200. For both of these reasons, the high energy electron population remains mostly constant until the proton density is significantly larger than its initial value.

During and immediately after the radius change, $T_{\text{e, low}}$ increases due to the increase in RMF power caused by the decrease in plasma volume. At this higher temperature, the rate of ionization increases, and the more numerous ionization losses cause $T_{\text{e, low}}$ to fall slightly. As the plasma becomes more and more ionized, the rate of ionization slows due to fewer neutral particles, allowing $T_{\text{e, low}}$ is to rise once again.

It is important to note that this model was designed to predict startup and likely does not properly include processes that are required to predict the steady state behavior of PFRC-2. Therefore, the behavior of the plasma post-peak ionization ($t > \sim 140\ \mu s$ in Fig 2.4) is not expected to be entirely correct.

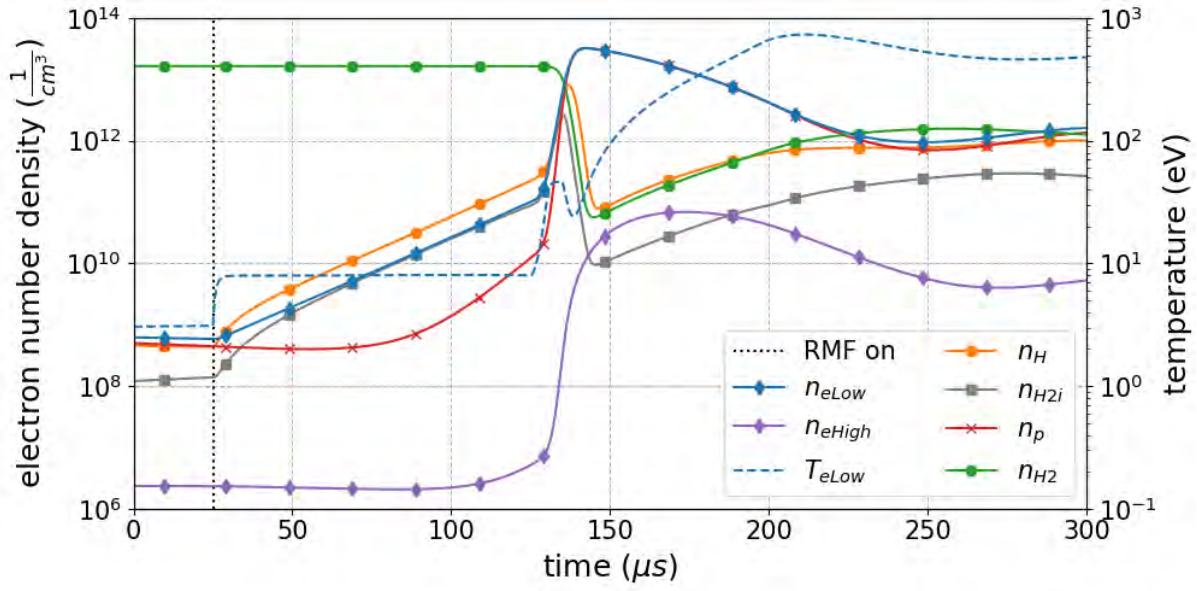

Figure 2.4: Example simulation run with the default parameters described in Sections 2.2 and 2.3. See Section 2.3.1 for an explanation of this plot

2.3.2 Comparison with Experiment

Shown in Fig 2.6 are simulations with parameters matching those of the experimental runs of Fig 2.5.[3] Comparing the simulated runs with the experimental runs, there are clear differences. Most notably, the experimental runs are much more closely clustered in time than the simulated runs. The only significant change in parameters between runs is the RMF power, so it appears my RMF-plasma coupling code is far from correct, causing the model to be overly sensitive to changes in $P_{\text{eff, RMF}}$. There are likely other deficiencies in the model that contribute to the difficulty in matching experiment, but in the presence of the erroneous RMF code, it is hard to diagnose other potential issues.

While this result does not bode well for the accuracy of the following results, it is worth noting that the simulation with $P_{\text{eff, RMF}} = 16$ kW was reasonably close to the relevant experimental run, so it would appear that the model is more accurate for higher values of $P_{\text{eff, RMF}}$.

[3]Please note that the RMF input powers listed in the legend of Fig 2.5 are the forward powers whereas the RMF power in the model is the effective absorbed power and is thus substantially smaller.

As stated above, the remainder of our simulations in this section sets $P_{\text{eff, RMF}} = 20$ kW (except when sweeping over RMF power), so results may be more accurate than implied by this subsection.

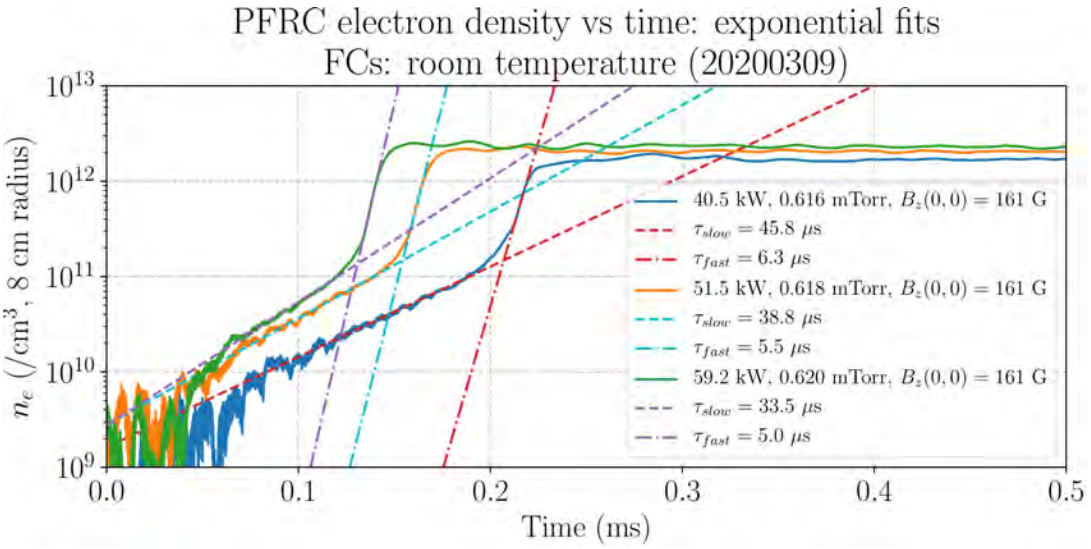

Figure 2.5: Plotted in the solid lines are the electron number densities of three PFRC-2 experimental runs vs time. Notice that during densification, n_e increases proportionally to $e^{t/\tau}$, where τ takes on two distinct values τ_{slow} and τ_{fast}. The dotted lines are fits that give the values for these time constants.

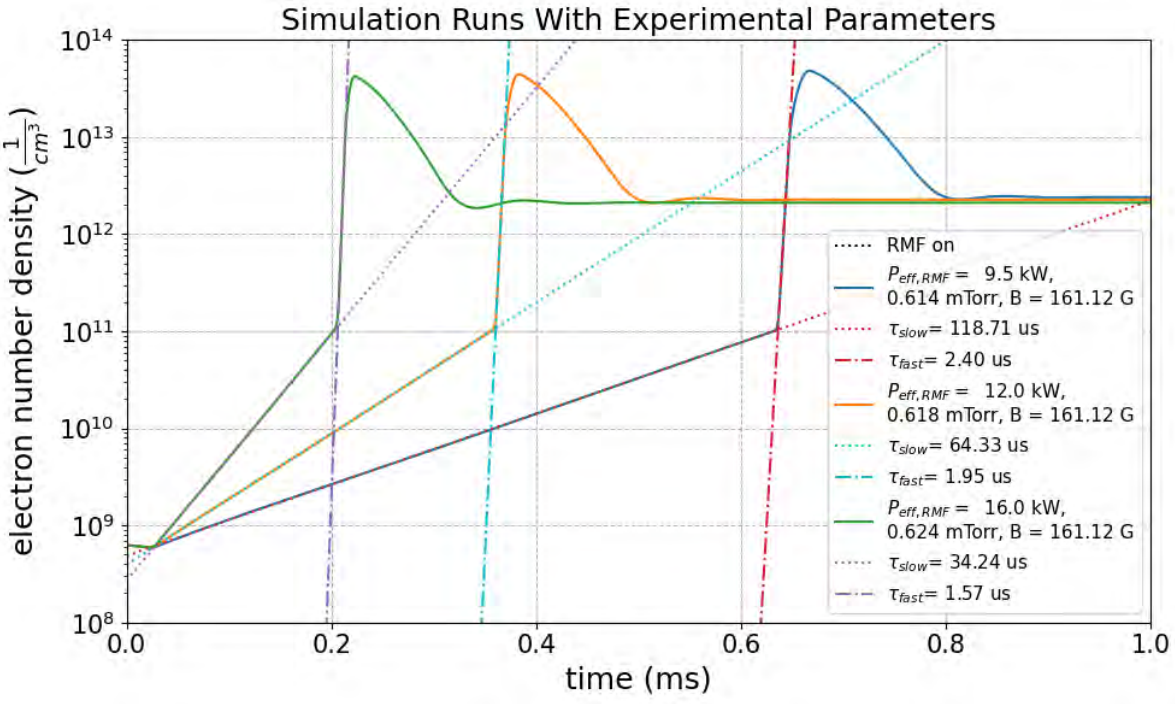

Figure 2.6: Simulations with the parameters matching those of the experimental runs shown in Fig 2.5.

2.3.3 Effects of High Energy Electrons

To illuminate the effect of the high energy electrons, I completed two sets of parameter sweeps. In the first set, high energy electrons were present, and in the second set, they were absent. The difference in the slow and fast timescales of densification between the two sets was then taken such that a negative difference corresponds to the timescale being smaller and hence faster with high energy electrons present. A positive difference would mean the opposite.

Beginning with a sweep over $P_{\text{eff, RMF}}$ (Fig 2.7 (a)), I found that the slow timescale was always faster when high energy electrons were present, but the phenomenon is less significant at higher RMF powers. This is likely because the ionization rate is already increased by the higher absorbed power, making the high energy electrons' effect less noticeable. The fast time scale exhibits the reverse behavior. The effect of the high energy electrons is lesser at low $P_{\text{eff, RMF}}$ and more pronounced at higher values.

Next, sweeping over the magnetic field strength (Fig 2.7 (b)), the slow timescale is found to generally be faster with high energy electrons present, but there are also values of B ($\lesssim 60$ G) where the high energy electrons lead to a slower slow timescale. The reason for why this occurs is currently unknown. Interestingly, the effect of high energy electrons is more pronounced at higher magnetic fields, where the confinement against Bohm losses is greater. The fast timescale behavior is rather odd, making it difficult to gain insight into how high energy electrons effect the fast timescale, but the majority of the curve is negative, so high energy electrons appear to generally quicken the fast region of densification.

Finally, I swept over the initial fill density (Fig 2.7 (c)). Much like the magnetic field sweep, the high energy electrons generally lead to a faster slow timescale, but there is a region ($n_{H_{2_0}} \lesssim 1.1 \cdot 10^{13}$ cm^{-3}) where high energy electrons are predicted to slow the slow timescale. Again, the reason for this is unknown. The fast timescale curve is largely negative except for a few spikes with the largest one being near $n_{H_{2_0}} = 1 \cdot 10^{13}$ cm^{-3}.

In the three comparison sweeps present in Fig 2.7, the fast timescale curve is noticeably less smooth than the slow timescale curve, and in the case of Fig 2.7 b, the fast timescale curve is especially strange. It may therefore be the case that our model does not predict the fast region of densification well. How physical these fast timescale curves are remains to be seen.

2.3.4 Parameter Sweeps

To now look at how specific parameters affect the startup process, additional parameter sweeps were created with the high energy electrons present. Beginning with sweeping over the magnetic field strength (Fig 2.8 (a)), both timescales of densification decrease with increasing magnetic field. This is believed to be due to greater confinement against Bohm losses with increasing field strength. Increased confinement leads to a greater number of electrons remaining in the plasma, meaning more ionization reactions occur, causing a more rapid densification. This idea is supported by the fact that the timescale curves appear to be rational functions of B, just like the Bohm diffusion coefficient $D_B \propto \frac{k_B T}{eB}$.

Next, sweeping over initial fill density (Fig 2.8 (b)), the general behavior is that while increased fill density produces a slower slow densification region, the fast densification region proceeds more rapidly. And from Fig 2.8 (c), increasing $P_{\text{eff, RMF}}$ decreases both timescales, as expected. Interestingly, there seem to be diminishing returns for higher values of $P_{\text{eff, RMF}}$.

Fig 2.8 (d) shows a sweep over the axial loss reducing factor, r_{reducing} (see section 2.2.1). As a reminder, a smaller r_{reducing} produces greater confinement. Similar to the magnetic field strength sweep, τ_{slow} decreases with increased confinement. It is difficult to discuss how the

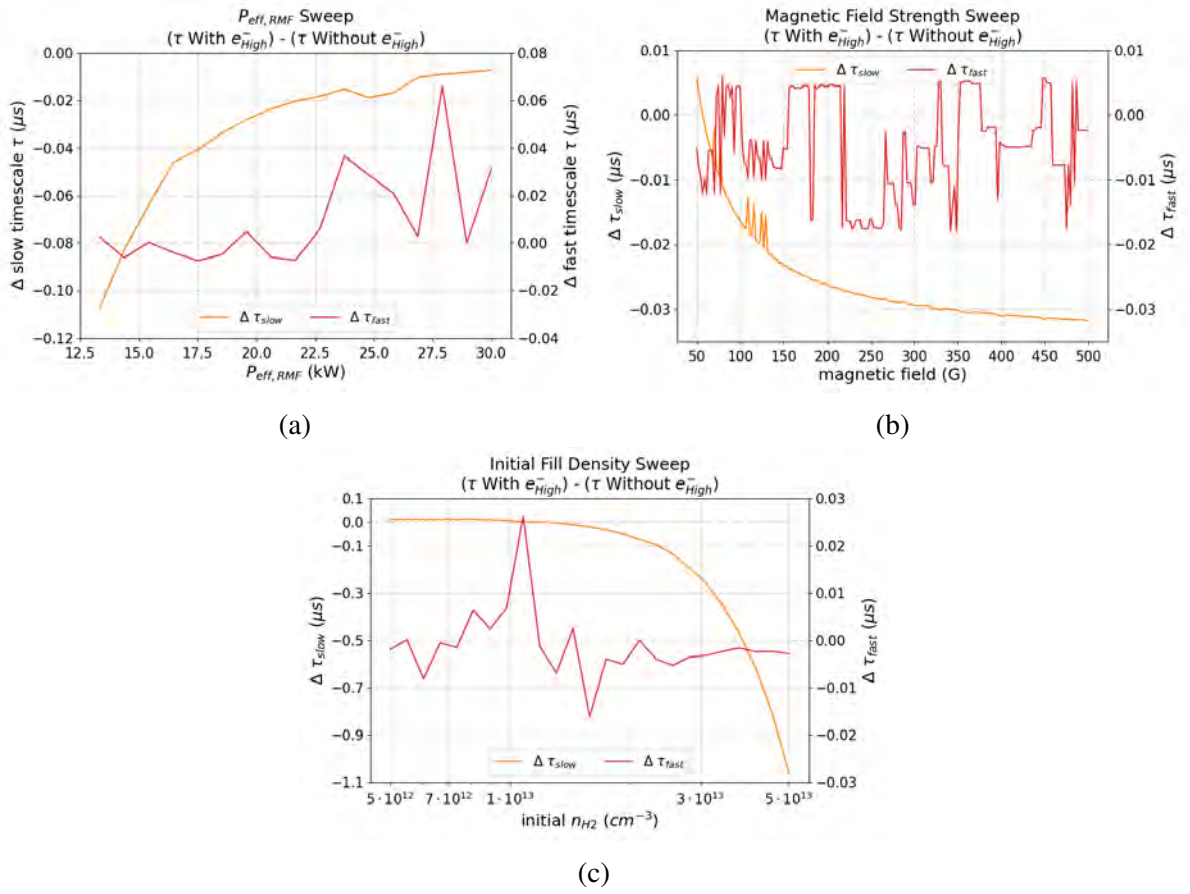

(a) (b)

(c)

Figure 2.7: Differences in the slow and fast timescales (τ_{slow} and τ_{fast}) between parameters sweeps with high energy electrons present and parameter sweeps without high energy electrons. The parameters swept over are the (a) RMF power, (b) magnetic field strength, and (c) initial fill density

fast timescale scales with r_{reducing} due to the high amount of variance, but it is perhaps generally trending downward with decreased confinement.

The final parameter sweep is over the gas puff rate (Fig 2.8 (e)). Below a puff rate of around 10^{15} cm^{-3}s^{-1}, gas puffs make little to no difference to the time scales. Above this value, gas puffs lead to a slower slow timescale, similar to the effect of increasing fill density. The fast timescale, on the other hand, first decreases before increasing at puff rates $\gtrsim 3 \cdot 10^{15}$ cm^{-3}s^{-1}.

Similar to the plots of Fig 2.7, the fast timescale curves of Fig 2.8 (a), (c), and (d) are noticeably less smooth than their slow timescale counterparts. This is further evidence that my code has issues simulating the fast densification region. However, it may be that the fast densification region is fundamentally different than the slow densification region, and these results are more correct than they appear.

2.4 Conclusion

I found that my model is overly sensitive to changes in $P_{\text{eff, RMF}}$ and cannot match the quantitative results of experiments. It is however able to produce the two timescales of densification by triggered a change in radius. Further development of our RMF-plasma coupling code is certainly required.

High energy electrons were found to generally make densification proceed more rapidly, but there were regions of parameter space where they slowed densification. What makes these regions special is currently unknown.

Densification appears to progress faster at higher levels of confinement, likely due to there being more electrons available to ionize neutrals, thereby freeing more electrons and creating a positive feedback cycle. Higher initial fill densities lead to slower slow timescales and faster fast timescales. As was expected, increasing $P_{\text{eff, RMF}}$ decreases both timescales, though there are diminishing returns at higher values of $P_{\text{eff, RMF}}$. Above gas puff rates of $\sim 10^{15}$ cm^{-3}s^{-1}, the fast timescale decreases and the slow timescale increases. At high puff rates $\gtrsim 3 \cdot 10^{15}$ cm^{-3}s^{-1}, the fast timescale then increases.

Future work may include adding a spatial dimension to better model plasma transport processes, adding nonadiabaticity of the magnetic moment (especially important for the high energy electrons[8]), dialing in free parameters, and further investigating RMF-plasma coupling.

2.5 Acknowledgements

I would like to thank Eugene Evans for answering my many, many questions and for patiently teaching me about plasma modeling, the PFRC group for providing great feedback and suggestions, and a huge thank you to Arturo Dominguez and Deedee Ortiz for somehow organizing a successful remote internship. This work was made possible by funding from the Department of Energy for the Summer Undergraduate Laboratory Internship (SULI) program. This work is supported by the US DOE Contract No. DE-AC02-09CH11466.

Bibliography

[1] S. A. Cohen, B. Berlinger, C. Brunkhorst, A. Brooks, N. Ferraro, D. P. Lundberg, A. Roach, and A. H. Glasser. Phys. Rev. Lett., **98**,145002, (2007).

[2] Michael Paluszek A.H. Glasser Gary Pajer, Yosef Razin and Samuel Cohen. (2012).

[3] Mr. Michael Paluszek, M. Thomas, and Mr. Yosef Razin. (2014).

[4] P. Jandovitz, C. Swanson, J. Matteucci, R. Oliver, J. Pearcy, and S. A. Cohen. Physics of Plasmas, **25**, (2018).

[5] Gabriel Gonzalez Jusino and Sam Cohen. (2019).

[6] Francis Chen. *Introduction to Plasma Physics and Controlled Fusion*. Springer, (2016).

[7] R.K. Janev, D.E. Post, W.D. Langer, K. Evans, D.B. Heifetz, and J.C. Weisheit. Journal of Nuclear Materials, **121**,10 – 16, (1984). ISSN 0022-3115.

[8] Charles Swanson. *Measurement And Characterization Of Fast Electron Creation, Trapping, And Acceleration In An Rf-Coupled High-mirror-ratio Magnetic Mirror*. PhD thesis, Princeton University, (2018).

[9] M. F. A. Harrison. *Atomic and Molecular Collisions in the Plasma Boundary*, pages 281–349. Springer US, Boston, MA, (1986).

[10] Folker Engelmann. *Introduction: Approaches to Controlled Fusion and Role of Plasma-Wall Interactions*, pages 15–39. Springer US, Boston, MA, (1986). ISBN 978-1-4757-0067-1.

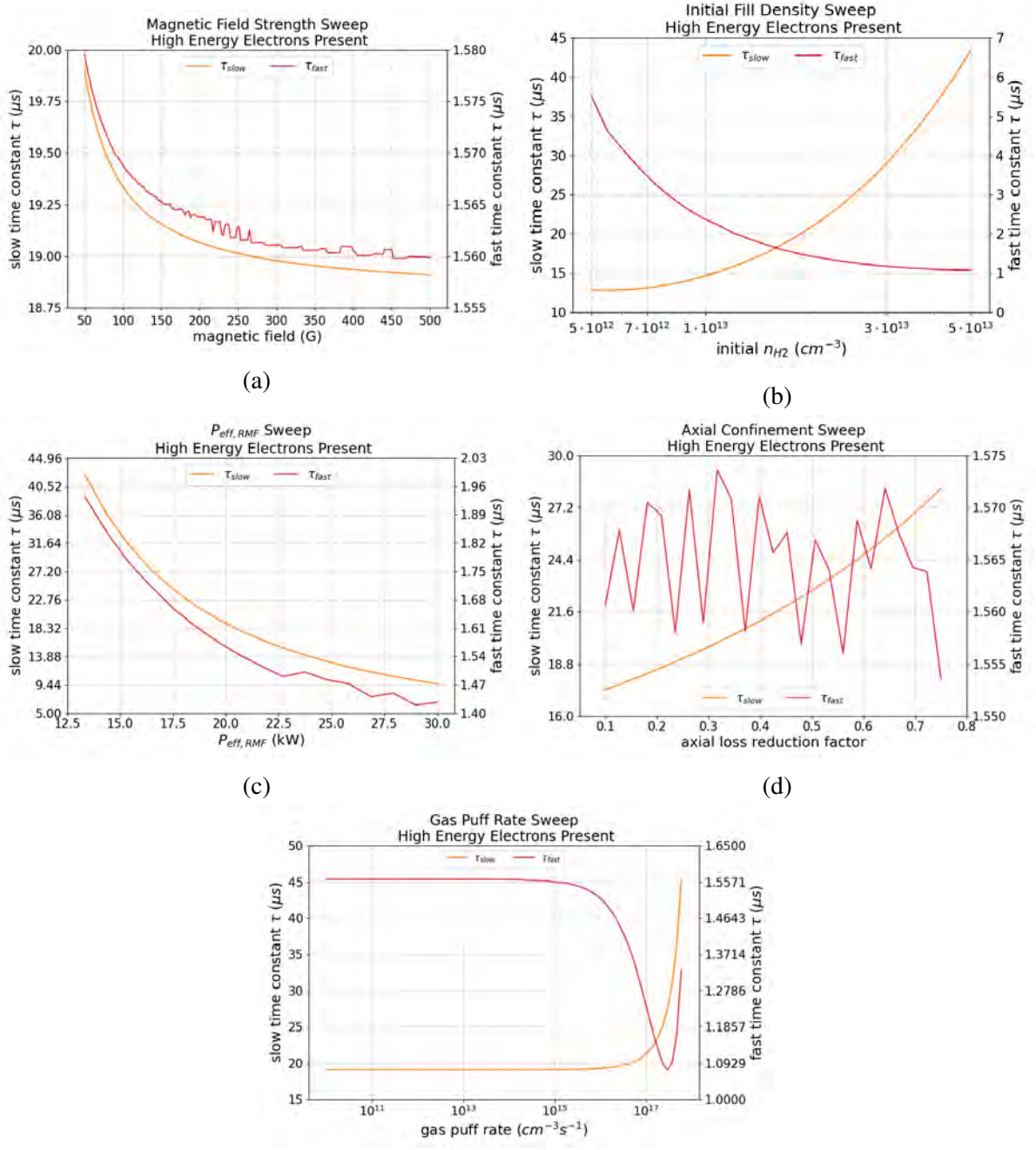

Figure 2.8: Parameter sweeps of the slow and fast timescales of densification ($\tau_{\text{slow}}, \tau_{\text{fast}}$) over (a) magnetic field strength, (b) initial fill density, (c) RMF power, (d) axial loss improvement factor, and (e) gas puff rate

Chapter 3

Scoping Study of Detecting High Harmonic Fast Waves in NSTX-U Hot Core Plasma Directly using Beam Emission Spectroscopy[1]

3.1 Introduction

The National Spherical Tokamak Experiment-Upgrade (NSTX-U), shown in Fig 3.1, is a fusion experiment at the Princeton Plasma Physics Laboratory (PPPL) investigating low aspect ratio tokamaks, also known as spherical tokamaks.[1,2] The aspect ratio of a tokamak (see Section 1.4.1 for a description of tokamaks) is defined as the ratio of the major radius to minor radius. The major radius is a measure of the total width of the device, and the minor radius is a measure of the width of a cross-section of the torus. The typical intuitive picture given for the effect of aspect ratio on the plasma shape is that a small aspect ratio causes the tokamak to look more like a cored apple while a high aspect ratio produces a donut shape. A diagram of the major and minor radii as well as a comparison between the shape of a high aspect ratio conventional tokamak (CT) and that of a low aspect ratio spherical tokamak (ST) can be found in Fig 3.2. The reason PPPL is researching STs is because of several advantages they possess over CTs. STs make more efficient use of space than CTs and can thus be built smaller, meaning they can be built more cheaply. Additionally, the geometry of their magnetic fields make STs more resistant against multiple kinds of magnetohydrodynamic instabilities than CTs. Though not within the scope of this thesis, instabilities are a large problem facing fusion, and a passive resistance to them would be beneficial. More information about the advantages of STs can be found in Peng et al. (1986)[3].

For the purposes of both heating and driving current, NSTX-U uses neutral beam injection (Section 1.5.2) as well as radio-frequency (RF) electromagnetic waves (Section 1.5.3). Currently, NSTX-U lacks the ability to locally measure the injected RF field and is thus unable to determine how the RF field is modified as it interacts with the plasma. This also means RF simulations are unable to be validated, resulting in a lower confidence in simulations and a de-

[1]This chapter is an adapted version of my paper of the same name that will be published as part of the Proceedings of the Virtual 23rd Topical Conference on High-Temperature Plasma Diagnostics. This work was completed with the help with Syun'ichi Shiraiwa, Dave Smith, and Nicola Bertelli.

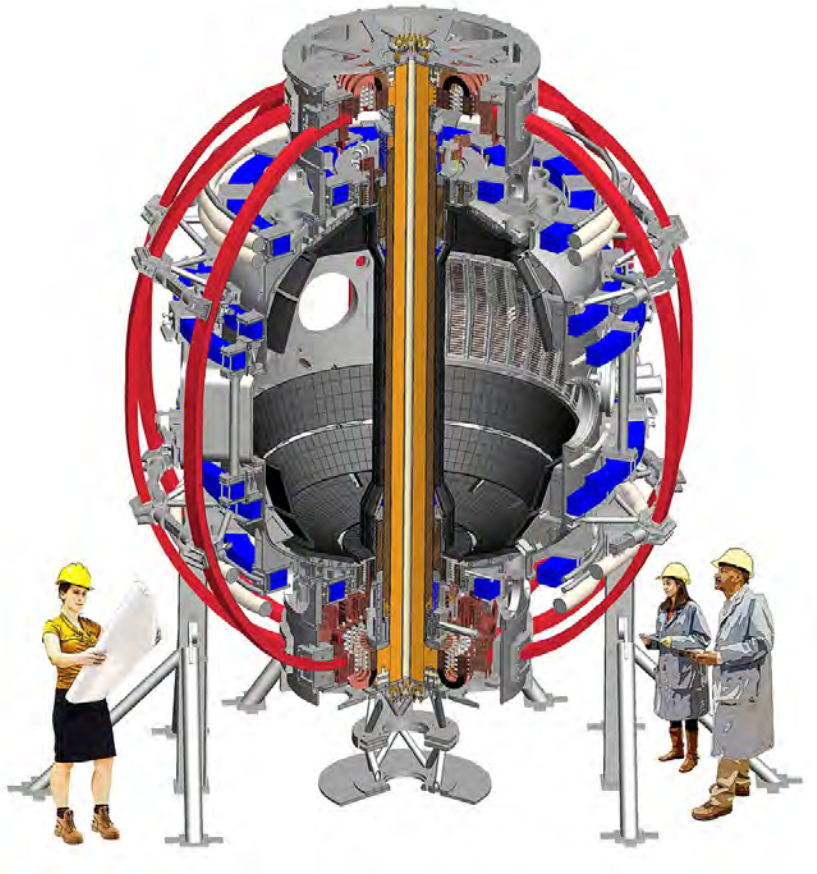

Figure 3.1: The National Spherical Tokamak Experiment-Upgrade (NSTX-U) **add citation**

creased capacity for simulations to contribute to the experiment. However, there is a potential method for locally measuring the RF field that has not yet been explored. Before discussing it further, a quick introduction to NSTX-U's RF system is necessary. The RF system consists of 12 antenna straps[2] extending 90° around the torus. To achieve greater efficacy in heating and driving current, antenna straps are often run out of phase relative to adjacent straps, meaning that the current passing through each strap is ϕ degrees behind the previous strap's current. Typical values of antenna phasing for NTSX-U are $30°, 90°,$ and $150°$.[5] The 12 straps are capable of injecting up to a combined 6 MW of 30 MHz high harmonic fast waves (HHFWs) into the plasma.[5,6] High harmonic fast waves are a type of electromagnetic wave whose angular frequency is many times that of the ion cyclotron frequency (see Section 1.4.1). The exact number of times larger the HHFW's angular frequency is than the ion's cyclotron frequency depends on where in the device one measures. An ion's cyclotron frequency, $\omega_{ci} = q_i B/m_i$, is a function of the magnetic field strength, which is not constant throughout a fusion reactor. In the case of NSTX-U, the angular frequency of the HHFWs is close to four times the cyclotron frequency of deuterons (the nucleus of a deuterium atom) for $B = 1$ T.

The potential method of evaluating the RF field is to first measure perturbations to the plasma density[3] induced by the RF fields and compare it to 3D RF calculations.[7] Unfortu-

[2] An antenna strap in this context is an antenna multiple times taller than it is wide with a curved shape to match the curvature of the toroidal plasma. The geometry of NSTX-U's antenna straps can be seen in Fig 3.4.

[3] This measurement is possible because fusion experiments typically have several diagnostics that measure plasma density as it is an important quantity both for understanding the physics (such as that of turbulence and particle transport) as well as for evaluating how close the experiment is to net energy.

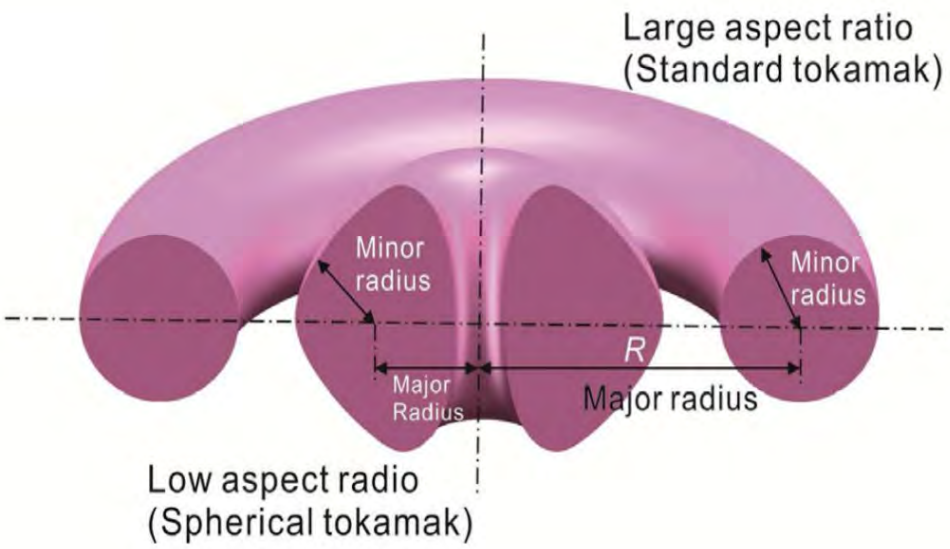

Figure 3.2: This diagram illustrates the major and minor radii of a tokamak and compares the geometry of a conventional tokamak to that of a spherical tokamak. [4]

nately, such measurements are often limited to the plasma edge since the density oscillation associated with the RF field is too fast compared to the typical frequency bandwidth of diagnostics systems. However, if HHFWs are launched at two slightly different frequencies f_1 and f_2, a beat wave will form with the resulting density oscillation occurring at the beat frequency $f_{beat} = f_1 - f_2 \approx 10$ kHz, which should be slow enough to measure.[8], [9]

To evaluate the density beat oscillation, 2D beam emission spectroscopy (BES) will be used.[10] BES observes spontaneous emission of collisionally excited neutral beam particles to measure perturbations in the local plasma density. The BES system of NSTX-U specifically observes Balmer-alpha lines produced by deuterium neutral beam particles with two collection optics, dubbed R130 and R140.[11] As of writing, only R140, the outermost optic is installed, and R130 is planned to be reinstalled around 2022. Fig 3.3 shows a simplified view of the BES system, illustrating the center lines of the three original neutral beams[4] (only the middle beam will be used for this measurement) and approximate fields of view of the optics. The true fields of view are shifted slightly towards the edge and are aligned to magnetic field pitch angles.

In this scoping study, the feasibility of generating and detecting the density beat oscillation is examined. I began by running 2D simulations of NSTX-U's midplane to develop trends in plasma parameters. I next moved to 3D for a more accurate geometry and to examine poloidal variations. Lastly, I created a synthetic diagnostic to take the 3D data and estimate the experimental 2D BES signal.

3.2 Simulations

All simulations were completed with Petra-M,[12,13] a 3D RF wavefield solver that uses the open source finite element library MFEM[14] to solve the wave equation

$$\nabla \times \frac{1}{\mu_0} \nabla \times \vec{E} - (\omega^2 \overleftrightarrow{K} + i\omega\sigma_{\text{coll}})\vec{E} = i\omega J_{\text{ext}}, \tag{3.1}$$

[4] Additional neutral beams were installed during the upgrade.

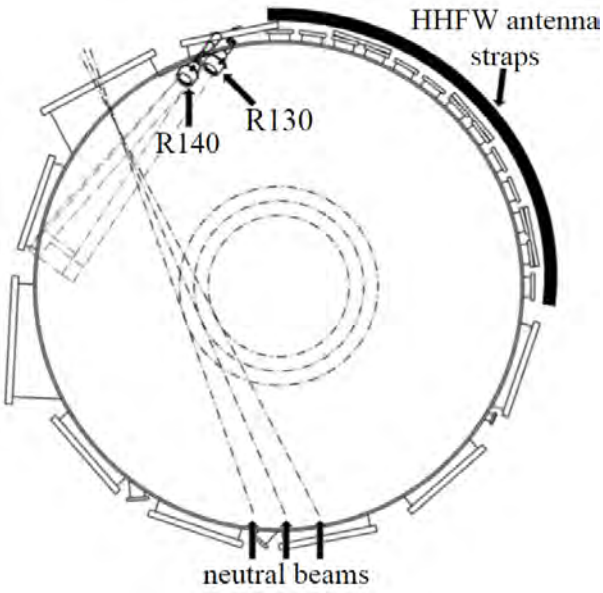

Figure 3.3: Top down view of the BES system at NSTX-U's midplane showing the center lines of the neutral beams and the fields of view of the R140 and R130 collection optics.

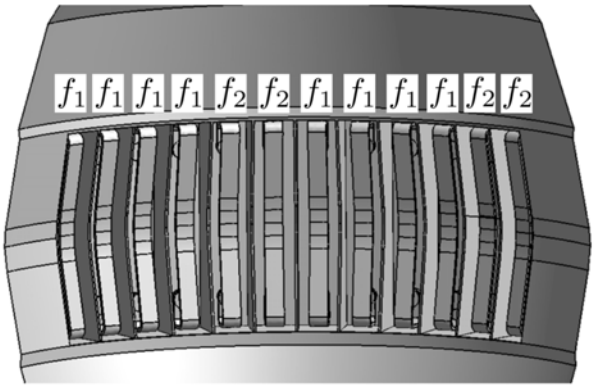

Figure 3.4: The frequencies of the 12 antenna straps in the 44-22 configuration.

where $\vec{E}$ is the RF electric field, ω is the angular frequency, $\overleftrightarrow{K}$ is the plasma dielectric tensor, σ_{coll} is an additional collision term (which can also be thought of as an additional conductivity term), and J_{ext} is the antenna current.

Unless stated otherwise, all simulations were run assuming a purely deuterium plasma with the default parameters of B = 1 T; $P_{RF} = 4$ MW; 90° antenna phasing; $T_e = T_i$; $f_1 = f_2 = 30$ MHz; and a parabolic background density profile with $n_{e0,\text{core}} = 5 \cdot 10^{19}\ m^{-3}$ and $n_{e0,\text{edge}} = 5 \cdot 10^{18}\ m^{-3}$. While the fields were evaluated with $f_1 = f_2 = 30$ MHz (this produced negligibly different fields compared to the true frequencies), when evolving the fields through time for the synthetic diagnostic (described in the last paragraph in this section), the correct frequencies of $f_1 = 30$ MHz and $f_2 = 30.01$ MHz $\Rightarrow f_{beat} = 10$ kHz were used. Additionally, I only considered the 44-22 antenna configuration (Fig 3.4) due to it having the cleanest spectrum out of all of the antenna groupings permitted by engineering constraints.

Due to the simpler geometry and smaller region to simulate, the 2D simulations had a much shorter runtime than the 3D simulations, allowing me to use them to quickly establish trends in various parameters. The 2D simulations were run with $\sigma_{coll} = 0$ and a parabolic temperature profile with $T_{core} = 1$ keV and $T_{edge} = 100$ eV. Additionally, the short runtime

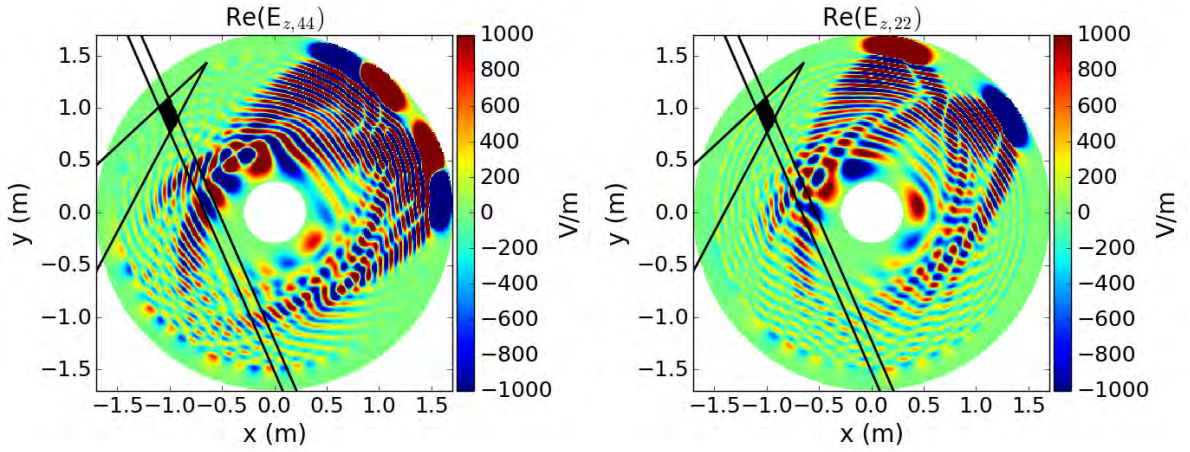

(a) (b)

Figure 3.5: Plotted is the real part of the z component (i.e. the component perpendicular to the page) of the RF electric field produced by the (a) 44 and (b) 22 antenna groups in a 2D simulation at $t = 0$. The real and imaginary (not pictured) portions are evolved through time according to $e^{it\omega_{44}}$ or $e^{it\omega_{22}}$. The neutral beam and the R140 field of view are bounded by the black lines, and the volume of measurement is the shaded region.

made it possible to use the plasma dielectric tensor given by Ono (1995) [15], which includes the dominant hot plasma terms for HHFWs. This is opposed to using the cold dielectric tensor, which assumes $T = 0$. The cold plasma dielectric tensor's advantage is its simplicity and thus its small contribution to a program's overall runtime. But because runtime was not an issue, a more accurate dielectric tensor was chosen instead. An example 2D simulation is shown in Fig 3.5, where the z component of the RF electric fields of the (a) 44 and (b) 22 antenna groups are plotted.

There are several inadequacies in the 2D simulations that necessitated 3D simulations. In 2D, I was unable to determine injected power due to unknown impedances in NSTX-U, and I therefore could not scale the simulation result to the desired power. More importantly, there is no poloidal extent, which is required for the synthetic diagnostic and also for some plasma phenomena to arise.

Due to a large jump in runtime from 2D to 3D, I used the cold plasma approximation instead of Ono's dielectric tensor to save time. In the cold approximation, particles are unable to damp waves and therefore cannot absorb power from them. To remedy this, σ_{coll} was set to 0.125. This was found to be an appropriate value by comparing cold 2D runs using different σ_{coll}s with a 2D simulation using Ono's dielectric tensor to see which σ_{coll} gave the best agreement.

Both the 2D and 3D simulations were ideal simulations and did not include the proper interaction between the edge of the plasma and the HHFWs. Experimentally, a greater amount of the power is deposited near the plasma edge than is predicted by my simulations.[5,16] Though I am currently unable to quantify this behavior, it will likely prove beneficial since the measurement volume is near the edge, and as I am about to show, $\delta n_{\text{beat}}/n_0 \propto \nabla^2(\text{Re}(\vec{E}_{f1}) \cdot \text{Re}(\vec{E}_{f2}))$.

While I was interested in both the electron and ion contribution to the beat fluctuation, I focused my simulation efforts on the electron fluctuation as I could readily derive an equation for $\delta n_{e,\text{beat}}/n_{e0}$ from the ponderomotive force, a nonlinear force arising from the radiation pressure of the high-powered RF field, on the electrons. Assuming no background electric or magnetic fields, this force is given by:[17]

$$\vec{F}_{NL} = \frac{-1}{4}\frac{q_e^2 n_e}{m_e \omega^2}\nabla(\text{Re}(\vec{E})^2), \tag{3.2}$$

where q_e is the electron charge, n_e is the local electron number density, m_e is the electron mass, ω is the angular frequency of $\vec{E}$, and $\vec{E} = (\vec{E}_{f1} + \vec{E}_{f2})$ is the RF electric field. Taking into account only the cross term, which represents the contribution of the beat wave generated by E_{f1} and E_{f2}, Eq 3.2 gives

$$\vec{F}_{NL} \rightarrow \frac{-1}{2}\frac{q_e^2 n_e}{m_e \omega_1 \omega_2}\nabla(\text{Re}(\vec{E}_{f1}) \cdot \text{Re}(\vec{E}_{f2})), \tag{3.3}$$

with $\omega_1 = 2\pi f_1$ and $\omega_2 = 2\pi f_2$.
Defining an electric field and its potential that give rise to the ponderomotive force using $\vec{F}_{NL} = q_e \vec{E}_{NL} = -q_e n_e \nabla \phi_{NL}$,

$$\nabla \phi_{NL} = \frac{1}{2}\frac{q_e}{m_e \omega_1 \omega_2}\nabla(\text{Re}(\vec{E}_{f1}) \cdot \text{Re}(\vec{E}_{f2})). \tag{3.4}$$

With Poisson's equation $\nabla^2 \phi = -\rho/\epsilon_0 = -q_e \delta n_{e,beat}/\epsilon_0$, this becomes

$$\frac{1}{2}\nabla^2(\text{Re}(\vec{E}_{f1}) \cdot \text{Re}(\vec{E}_{f2})) = \frac{-m_e \omega_1 \omega_2}{\epsilon_0}\delta n_{e,\text{beat}}. \tag{3.5}$$

After rearranging terms and substituting in the electron plasma frequency ω_{pe}, the equation for the electron density beat oscillation is obtained:

$$\frac{\delta n_{e,\text{beat}}}{n_e} = \frac{-q^2}{\omega_1 \omega_2 \omega_{pe}^2 m_e^2}\frac{1}{2}\nabla^2(\text{Re}(\vec{E}_{f1}) \cdot \text{Re}(\vec{E}_{f2})). \tag{3.6}$$

Due to the low frequency of the beat oscillation (10 kHz), quasineutrality (see Section 1.1) is expected to produce an ion beat fluctuation of similar magnitude (though the phase may differ) as the electron beat fluctuation. For the remainder of this chapter, I will therefore consider $\delta n_{e,beat}/n_e$ to be an upper bound on $\delta n_{i,beat}/n_{i,0}$ and $\delta n_{beat}/n_0$.

To estimate the experimental 2D BES signal the beat fluctuation will produce, I developed a synthetic diagnostic by first approximating the measurement volume of each R140 sightline (Fig 3.6) as the intersection of the neutral beam volume and a cylinder around the sightline axis. E_{f1} and E_{f2}, as calculated by Petra-M, are then evolved through time to obtain the time series of the average $\delta n_{e,\text{beat}}/n_{e0}$ within each sightline, the amplitudes of which can be compared against the sensitivities of the BES system. Next, the cross-correlations of the time series relative to the upper leftmost sightline (arbitrarily chosen) are taken, as defined by $C(g_{\text{UL}}, g_2) = \sum_{t=0}^{T} g_{\text{UL}}^*(t) g_2(t+\tau)$, where g_{UL} is the time series of the upper leftmost sightline, g_2 is another sightline's time series, τ = 0, t is a given point in time, and T is the final point in the time series. Lastly, these cross-correlations are Fourier transformed to obtain a k_z and a k_r spectrum. These spectra can be found experimentally, and if they match those given by the synthetic diagnostic, the correct oscillation is likely being measured.

3.3 Results

Using 2D simulations of NSTX-U's midplane, I established trends in B, T_{core}, $n_{e0,\text{core}}$, and phasing between adjacent antenna straps for the overall average $\delta n_{e,\text{beat}}/n_{e0}$. These trends

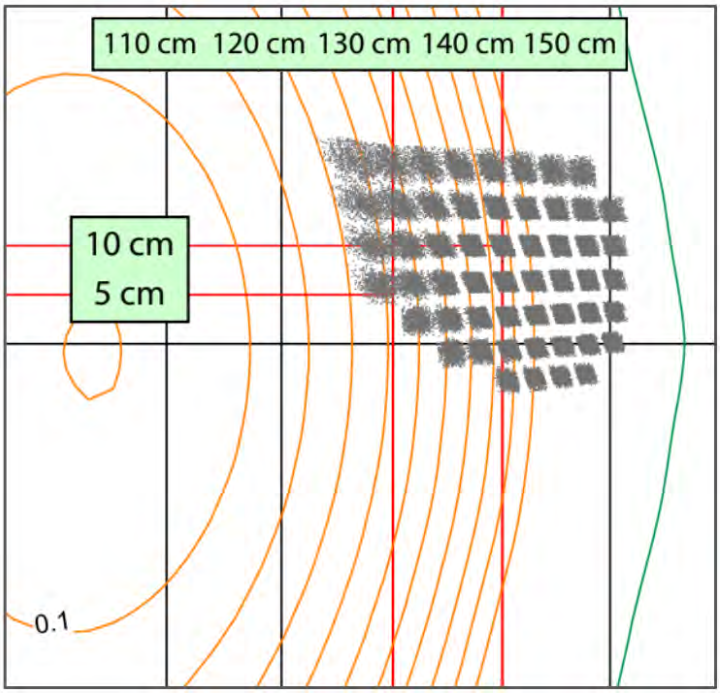

Figure 3.6: Plotted is the outer half of a cross section of NSTX-U to show intersections between R140's sightlines and the center of the neutral beam, as projected onto the r-z plane.[18] r is the direction outwards from the central hole of the tokamak and z is the vertical direction with $z = 0$ set to the midplane of the device. The poloidal magnetic field lines are drawn in orange, and the wall of the reactor is shown in green.

are shown in Figs 3.7 (a), (b), (c), and (d), respectively, and are normalized to the $\delta n_{e,\text{beat}}/n_{e0}$ produced by the default parameters listed in Section 3.2. The associated trend lines were calculated via a linear regression after taking the log of the data. Looking to these plots, the data points form fairly straight lines on a log scale and do not vary widely from the trend lines, so it appears that $\delta n_{e,\text{beat}}/n_{e0} \propto e^{B}, e^{-n_{e0,\text{core}}}, e^{-T_{core}}$, and $e^{-\text{phasing}}$.

The current explanation for these trends is that they correspond to decreasing wave absorption, thus increasing the RF electric amplitude and its derivatives. Given that $\delta n_{e,\text{beat}}/n_{e0} \propto \nabla^2(\text{Re}(\vec{E}_{f1}) \cdot \text{Re}(\vec{E}_{f2}))$, decreasing wave absorption also leads to a larger $\delta n_{e,\text{beat}}/n_{e0}$. These trends reflect this because: Increasing B decreases wave absorption since damping scales with $\beta \propto 1/B^2$;[19] At higher temperatures, each plasma particle is able to damp the wave to a greater degree, and at higher densities, there are more particles present to absorb power from the waves; Lastly, increasing antenna phasing increases Landau damping,[20,21] a type of wave-particle resonance and a major way in which HHFWs interact with the plasma.[15] Thus, $\delta n_{e,\text{beat}}/n_{e0}$ will be maximized in a high field, low density, low temperature plasma with small phasing between antenna straps, making this the optimal plasma in which to attempt the measurement.

In a 3D simulation using default parameters, the average magnitude of $\delta n_{e,\text{beat}}/n_{e0}$ over all sightlines ranged from about $5 \cdot 10^{-10}$ to 10^{-9} throughout the time series. Comparing this to the BES sensitivity of $\delta n/n \gtrsim 10^{-4}$,[22,23] it at first appears that the desired measurement is not possible. However, assuming that the 2D trends presented in Fig 3.7 are independent of one another and also hold in 3D, by varying parameters, $\delta n_{e,\text{beat}}/n_{e0}$ could be increased by a factor of about 10^6, putting it in the range potentially measurable by BES. But this does not consider any experimental constraints that will inhibit NSTX-U's ability to vary parameters.

The k_z and k_r spectra associated with the default 3D simulation (blue curve) and an addi-

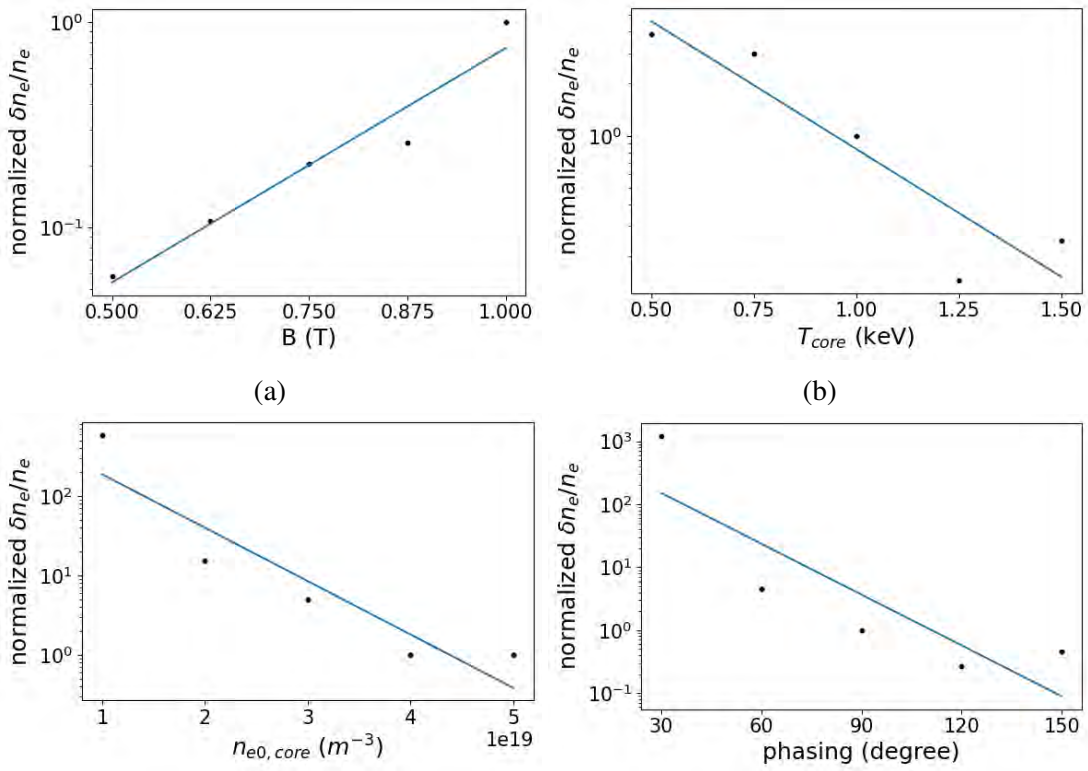

Figure 3.7: Trends of $\delta n_{e,\text{beat}}/n_e$ produced by the 2D simulations in (a) B, (b) T_{core}, (c) $n_{e0,core}$, and (d) antenna phasing. All data points are normalized to the point corresponding to default parameters listed in Section 3.2

.

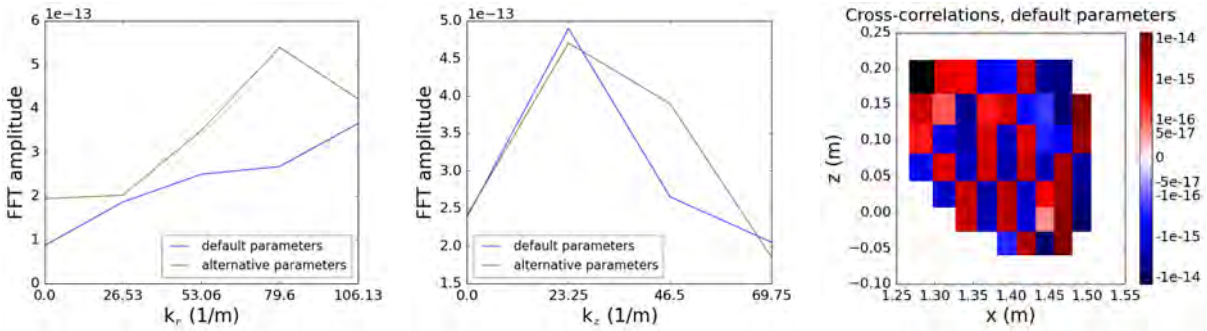

(a) (b) (c)

Figure 3.8: (a,b) The k_r and k_z spectra, respectively, produced by Fourier transforming the cross-correlation data of the default case and the alternative parameter case. See Section 3.2 for the default parameters and Section 3.3 for the alternative parameters. (c) The cross correlations of the average $\delta n_{e,\text{beat}}/n_{e0}$ time series at each of the R140 sightlines (Fig 3.6) relative to the upper leftmost sightline (in black) using the default parameters listed in Section 3.2.

tional simulation (green curve) with alternative parameters of $B = 0.5$ T; $n_{e0,\text{core}} = 4 \cdot 10^{19}$ m^{-3}; $n_{e0,\text{edge}} = 4 \cdot 10^{18}$ m^{-3}; and $P_{RF} = 6$ MW are shown in Fig 3.8 (a) and (b). These alternative parameters were chosen because they are notably different than the default parameters but remain in or near NSTX-U's accessible parameter space. Both k_z spectra and the alternative k_r spectrum are peaked, which makes them easier to measure than monotonically increasing or decreasing spectra and will aid in the comparison between experimental and simulated spectra. Looking at the default and alternative spectra, they are similar but not overly so. Thus, one may expect the spectra produced by the parameters required to achieve $\delta n_{e,\text{beat}}/n_{e0} > 10^{-4}$ will significantly differ from the default case. Additionally in Fig 3.8 (c) are the cross-correlations for the default 3D simulation, giving an example of the sort of spatial structures in the RF field that may be observable with the 2D BES system.

3.4 Conclusion

Utilizing recent developments in full wave simulation, I established trends in B, T_{core}, $n_{e0,\text{core}}$, and antenna phasing for the average $\delta n_{e,\text{beat}}/n_{e0}$ over all sightlines. Specifically, I found that $\delta n_{e,\text{beat}}/n_{e0} \propto e^{B}, e^{-n_{e0,\text{core}}}, e^{-T_{\text{core}}}$, and $e^{-\text{phasing}}$. Consequently, the density beat oscillation will be easiest to measure in a high field, low density, low temperature plasma with small phasing between antenna straps. The $\delta n_{e,\text{beat}}/n_{e0}$ predicted by the default 3D simulation is several orders of magnitude smaller than the BES sensitivities, but changing parameters as suggested by the 2D trends may raise the amplitude substantially. The k_r and k_z spectra for 3D simulations with the default and an alternative set (described in Section 3.3) of parameters were calculated. Both k_z spectra and the alternative k_r spectrum exhibited peaks that will be useful in comparing the experimental and simulated spectra.

Following resumption of NSTX-U operations and RF experiments in 2022, this measurement will be attempted in order to hopefully provide the capability of identifying the injected RF field. The installation of the R130 sightline in 2022 will aid this measurement as its field of view is closer to the core, where the RF field amplitude is larger, but future work should be done to determine how beneficial this effect will be.

Should it become apparent that measuring the beat fluctuation with BES is not feasible, the measurement could be attempted with other diagnostics as well, such as with NSTX-U's ultrasoft X-ray imaging system.[24] This diagnostic has a lower sensitivity than BES, but its field of view contains a region of much higher RF field amplitude, which would likely make up for the lower sensitivity.

Acknowledgements

I would like to thank Syun'ichi Shiraiwa and Nicola Bertelli of the Princeton Plasma Physics Laboratory and Dave Smith of the University of Wisconsin-Madison for all of their assistance throughout this project. This work was supported by the U.S. Department of Energy, Office of Science, Office of Fusion Energy Sciences Award No. DE-SC0001288 and by the U.S. Department of Energy Contract No. DE-AC02-09CH11466. This research used resources of the National Energy Research Scientific Computing Center (NERSC), a U.S. Department of Energy Office of Science User Facility operated under Contract No. DE-AC02-05CH11231.

Bibliography

[1] J.E. Menard *et al.* Nuclear Fusion, **52**, 083015, (2012).

[2] J.E. Menard *et al.* Nuclear Fusion, **57**, 102006, (2017).

[3] Y-K.M. Peng and D.J. Strickler. Nuclear Fusion, **26**,769–777, (1986).

[4] Kulagin, V.V. *http://plasma.mephi.ru/ru/uploads/files/Seminars/20200520%20SferTokamak/20200520%20Kulagin%20V.V._Compact%20magnetic%20confinement%20fusion%20Spherical%20torus%20and%20compact%20torus%20[1].pdf*, (2020).

[5] J. Hosea *et al.* Physics of Plasmas, **15**, 056104, (2008).

[6] J. R. Wilson *et al.* Physics of Plasmas, **10**,1733–1738, (2003).

[7] T. Intrator *et al.* Physics of Plasmas, **3**, 1331–1339, (1996).

[8] H.P. Laqua *et al.* Nuclear Fusion, **58**, 104003, (2018).

[9] M. Saigusa *et al.* Nuclear Fusion, **42**, 412–417, (2002).

[10] R. J. Fonck *et al.* Review of Scientific Instruments, **61**,3487–3495, (1990).

[11] D. R. Smith *et al.* Review of Scientific Instruments, **81**,10D717, (2010).

[12] Shiraiwa, S. *et al.* EPJ Web Conf., **157**, 03048, (2017).

[13] N. Bertelli *et al.* AIP Conference Proceedings, **2254**,030001, (2020).

[14] R. Anderson *et al.* Computers & Mathematics with Applications, (2020).

[15] Masayuki Ono. Physics of Plasmas, **2**, 4075–4082, (1995).

[16] R. J. Perkins *et al.* Phys. Rev. Lett., **109**, 045001, (2012).

[17] Francis Chen. *Introduction to Plasma Physics and Controlled Fusion*, page 285. Springer, (2016).

[18] D. Smith. High Temperature Plasma Diagnostics Conference, Madison, WI, (June 2016).

[19] S.C. Chiu *et al.* Nuclear Fusion, **29**, 2175–2186, (1989).

[20] C. N. Lashmore-Davies *et al.* Physics of Plasmas, **5**,2284–2290, (1998).

[21] N. Bertelli *et al.* Nuclear Fusion, **59**, 086006, (2019).

[22] D. R. Smith *et al.* Review of Scientific Instruments, **83**,10D502, (2012).

[23] D.R. Smith *et al.* Nuclear Fusion, **53**, 113029, (2013).

[24] D. Stutman *et al.* Review of Scientific Instruments, **70**,572–576, (1999).